RESEARCH MEMORANDUM

STABILITY OF TWO ROCKET-PROPELLED MODELS HAVING ASPECT-RATIO-5 UNSWEPT TAILS ON A LONG BODY FOR THE MACH NUMBER RANGE OF 1.7 TO 2.4

By Reginald R. Lundstrom

Langley Aeronautical Laboratory
Langley Field, Va.

NATIONAL ADVISORY COMMITTEE
FOR AERONAUTICS

WASHINGTON

March 27, 1957

NATIONAL ADVISORY COMMITTEE FOR AERONAUTICS

RESEARCH MEMORANDUM

STABILITY OF TWO ROCKET-PROPELLED MODELS HAVING ASPECT-RATIO-5 UNSWEPT TAILS ON A LONG BODY FOR THE MACH NUMBER RANGE OF 1.7 TO 2.4

By Reginald R. Lundstrom

SUMMARY

Two rocket models having cruciform, aspect-ratio-5, unswept tails and a fineness-ratio-20 fuselage were flight tested over a Mach number range of approximately 1.7 to 2.4. One of the models had cruciform, aspect-ratio-3.4 forward surfaces in line with the tails. The models were given step disturbances by pulse rockets at intervals throughout the Mach number range and stability derivatives were obtained from the measured responses. The roll rates of the models varied from 10 radians per second to 5 radians per second.

The measured lift-curve slopes in the plane in which the disturbance originated (pitch) were much lower than the lift-curve slope in the other plane (yaw) for both models. The measured lift-curve slopes in the pitch plane were in good agreement with potential-flow theory. The damping of the model with tail only was greater than that predicted by theory. The damping of the model with both forward surfaces and tails was about the same as that predicted by theory. The aerodynamic center of both models was farther forward than was predicted by potential-flow theory.

INTRODUCTION

As the speed of missiles has advanced far into the supersonic regime, the general tendency has become more and more to use wings of low aspect ratio. This trend is a logical one since the increase in lift-curve slope with aspect ratio has become very small at Mach numbers of 2 and above, and the elastic problems of a high-aspect-ratio wing at high speed become rather severe. As a result, very little experimental data has been obtained or needed on high-aspect-ratio wings in this speed range.

Recently, however, with the advent of folding-fin rockets as airplane armament, high-aspect-ratio wings at Mach numbers around 2 become of interest. The chord is restricted in order to allow the fins to fold readily and a comparatively large span is often necessary to have sufficient stabilizing area. It is conceivable that guidance systems may be developed which can be fitted in small aircraft rockets and will require a rather blunt nose body. Such a missile will probably have a high-fineness-ratio fuselage and forward-control fins since the rear part of the fuselage will be, of necessity, a rocket motor.

Adequate theory exists for calculating the lift-curve slope and aerodynamic center of such a high-aspect-ratio configuration in a supersonic potential flow. (For example, see refs. 1 and 2.) A question exists as to whether the assumption of potential flow is valid for all conditions that may be encountered by guided aircraft rockets. The purpose of the present investigation is to compare stability derivatives obtained experimentally at high Reynolds number with stability derivatives calculated from existing theory for a possible folding-fin configuration. Experimental static and dynamic stability data as obtained from two free-flight models are presented. The fuselages of both models had hemispherical noses and body fineness ratios of 20. The cruciform tail surfaces of both models were unswept and untapered and had an aspect ratio of 5. One of the models had cruciform lifting surfaces on the forward part of the missile such as might be used for control fins. The models were disturbed at predetermined intervals during their flights by small rockets firing normal to the model flight path. Dynamic and static stability derivatives as calculated from the measured responses of the missiles to these disturbances are compared with the derivatives as calculated from potential-flow theory.

SYMBOLS

A_n normal acceleration, g units

A_t transverse acceleration, g units

C_D drag coefficient, $\frac{\text{Drag}}{q\pi r^2}$

C_m pitching moment about model center of gravity, $\frac{\text{Pitching moment}}{qS\bar{c}}$

C_N normal-force coefficient

C_L lift coefficient

[redacted]

C_R	resultant-force coefficient
C_Y	side-force coefficient
I_X, I_Y, I_Z	moments of inertia about X-, Y-, and Z-axes, respectively, slug-ft^2
K_M	space motion factor (used in ref. 5)
p_t	total pressure, lb/sq in.
R	Reynolds number per foot
V	free-stream velocity, ft/sec
X,Y,Z	body coordinate axes
b	span of tail surfaces (used only in pb/2V), ft exponential damping constant in e^{-bt}, per second
$\bar{c}$	mean aerodynamic chord, ft
g	acceleration due to gravity, 32.2 ft/sec^2
m	model mass, slugs
p	roll rate, radians/sec
q	dynamic pressure, lb/sq ft
S	exposed tail area in one plane, sq ft
t	time from model launching, sec
r	body radius, ft
x	distance from center of pressure of air-flow indicator to model center of gravity (4.74 ft for both models)
α	angle of attack of model, deg
α_i	angle of attack indicated by flow-direction indicator, deg
β	angle of sideslip of model, deg
β_i	angle of sideslip indicated by flow-direction indicator, deg

[redacted]

$\dot{\theta}$ pitching velocity, radians/sec

$\dot{\psi}$ yawing velocity, radians/sec

ω damped natural frequency of resultant motion, radians/sec

Subscripts:

q derivative with respect to $\dot{\theta}\bar{c}/2V$

α derivative with respect to α

$\dot{\alpha}$ derivative with respect to $\dot{\alpha}\bar{c}/2V\left(\frac{1}{57.3}\right)$

β derivative with respect to β

$\dot{\beta}$ derivative with respect to $\dot{\beta}\bar{c}/2V\left(\frac{1}{57.3}\right)$

t indicates value at trim condition

A dot over α or β indicates a derivative with respect to time.

MODELS AND APPARATUS

Model Description

The models used for these tests had fuselage fineness ratios of 20 and cruciform tails of aspect ratio 5 that were untapered and unswept. One model, referred to throughout this report as model 1, had no forward surfaces. The other model, referred to in this report as model 2, was identical in configuration to model 1 except for the addition of aspect-ratio-3.4 cruciform forward surfaces arranged in line with the tail. A general arrangement of both models is shown in figure 1 and details of the lifting surfaces are shown in figure 2. The telemeter antennas shown in figures 1 and 2 and the total-pressure tubes shown in figure 1 were indexed 45° with respect to the tails in an effort to minimize interference. The air-flow direction pickups located in front of the models were believed to be located far enough forward to minimize their windshield effect on the blunt hemispherical noses. The fuselage forward section was made of 3/16-inch wall-steel tubing and the rear section was a standard 5-inch HVAR rocket motor. The solid-steel fins were welded to the fuselage. It is believed that the models were sufficiently rigid; thus, effects of flexibility were negligible. Photographs of the models are presented in figure 3. The dimensional and mass data are as follows:

[redacted]

Exposed tail area (per plane), sq ft	0.6944
Fuselage cross-sectional area, sq ft	0.1363
Exposed forward wing area (model 2 only), per plane, sq ft	0.4167
Tail mean aerodynamic chord, ft	0.4167
Center-of-gravity position (both models), inches from nose	43.9

	Model 1 (fuel burned)	Model 2 (fuel burned)
Weight, lb	162.1	168.6
I_X, slug-ft^2	0.293	0.32
I_Y or I_Z, slug-ft^2	38.9	39.4
$\frac{I_X}{I_Y}$	0.0075	0.0081

INSTRUMENTATION

The models were equipped with an NACA eight-channel telemeter which transmitted a continuous record of normal, transverse, and longitudinal acceleration, pitch angular acceleration, roll rate, total pressure, angle of attack, and angle of sideslip. No reliable information was received from the pitch angular acceleration pickup on either model.

Velocity was measured by a CW Doppler velocimeter and the positions of the models in space were measured with an NACA modified SCR 584 tracking radar set. Atmospheric temperature, pressure, wind velocity, and wind direction were measured by a Rawinsonde. The method of reference 3 was used in an attempt to launch the models on a day when the atmospheric turbulence was low.

Test Technique

The models were launched from a near-zero-length mobile launcher at an elevation angle of 45°. Each model was boosted to supersonic velocity by a first-stage booster powered by two 6-inch-diameter solid-propellant rocket motors which together produced approximately 12,000 pounds of thrust for 3 seconds duration. The 5-inch HVAR rocket motor which made up the rearward part of each of the model fuselages was fired directly after first-stage burnout, separated the model and booster, and propelled the model up to a maximum speed. As the models coasted down through the Mach number range, four small rockets on each model were fired normal to the flight path at intervals in order to cause free pitch oscillations of the models. These small rockets, referred to as pulse rockets, delivered 20 pound-seconds of impulse over about 0.06 second.

PRECISION OF DATA

The velocity data, as obtained by the CW Doppler velocimeter, were corrected for flight-path curvature and for wind effects at altitude. The angle of attack α and angle of sideslip β at the model center of gravity were obtained from the wind-flow-direction indicator by using the following relationships:

$$\alpha = \alpha_1 + \frac{x}{V}\left(\dot{\alpha}_i + \frac{(57.3)(32.2)A_n}{V} + \beta_1 p\right)$$

$$\beta = \beta_i + \frac{x}{V}\left(\dot{\beta}_i - (57.3)(32.2)\frac{A_t}{V} - \alpha_1 p\right)$$

Since all linear accelerometers obviously could not be located at the model center of gravity, corrections had to be applied for angular velocities and accelerations. These corrections were very small, in almost all cases being less than 1 percent of the instrument range.

ACCURACY

The accuracy of the instrumentation used for these tests should cause the following quantities to be within the following incremental limits for the two Mach numbers listed:

Mach number	$\alpha - \alpha_t$ or $\beta - \beta_t$	C_N or C_Y	C_D	p
2.4 ± 0.02	±0.15	±0.003	±0.05	±0.2
1.7 ± 0.02	±0.15	±0.005	±0.07	±0.2

The absolute values of α and β which are not used for results in this report are not nearly as accurate as $\alpha - \alpha_t$ and $\beta - \beta_t$ because of possible fin misalinements of the air-flow indicator. No rigorous assessment of the accuracy of the stability derivatives can be obtained. In the method used for determining C_{N_α}, the random errors and some of the systematic errors are canceled out when the slope is determined. In the case of C_{m_α} and $C_{m_q} + C_{m_{\dot{\alpha}}}$, the linearity of the derivative itself is often very questionable. The following listed accuracies are based on limited experience from instances when several similar models of a configuration have been tested or when checks with other methods have been possible:

C_{N_α} or C_{Y_β}, percent	±5
C_{m_α}, percent	±8
$C_{m_q} + C_{m_\alpha}$, percent	±20

RESULTS AND DISCUSSION

All coefficients presented in this report with the exception of C_D are based on the exposed area of the tail in one plane (0.6944 sq ft) and the tail chord (0.4167 ft). All moment coefficients are referred to the model center of gravity (43.9 inches from model nose). The drag coefficient C_D is based on the fuselage cross-sectional area. The variation of Reynolds number per foot with Mach number for the tests is shown in figure 4. The measured total-pressure variation with time for model 1 is presented in figure 5 along with a calculated value obtained by using Rayleigh's supersonic pitot equation. The Mach number and static pressure used in the pitot equation were obtained from the CW Doppler and SCR 584 radar and Rawinsonde measurements. When compared, the measured and calculated total pressures for model 2 appeared to be very much like those shown for model 1. For both models the agreement below a Mach number of 1.9 is very good but above a Mach number of 1.9 the measured total pressure is lower and very irregular. This result suggests that, above $M = 1.9$, the total-pressure tube is in a region of separated flow and it seems logical that at other positions around the fuselage there may also at times be a separated flow. Attempts to correlate the irregularities in the measured total pressure with variations in α and β showed nothing that appeared systematic but they were evident even at angles of attack of less than 1°. Occurrences of this nature, of course, are strongly dependent on the Reynolds number of the test.

Time Histories

The time history of C_N, C_Y, roll rate, and Mach number during pulse-rocket firings is shown in figures 6 and 7 for models 1 and 2, respectively. Note the irregular response of C_N and C_Y because of their being referenced to a conventional body-axis system while the model is rolling at from 5 to 10 radians per second. Little evidence of cross coupling is apparent on the roll-rate trace because of the small angles of attack and sideslip (usually less than 2°). The rather abrupt steps on the roll-rate trace occur when the pulse rocket fires, since the thrust line of the pulse rockets was not in the X,Z plane but was parallel to it and displaced 0.75 inch. The average variation of $pb/2V$ with Mach number is shown in figure 8 to be approximately constant for model 2

but increasing with Mach number for model 1. The roll rate could not be accurately predicted from fin misalinement. From measured wing misalinements, model 1 was calculated to have had a value of $pb/2V$ of -0.0021 during flight test. Similarly, the effects of wing-tail interference being neglected, model 2 was calculated to have had a value of $pb/2V$ of 0.0010.

Normal Force Due to Angle of Attack

Plots of C_N against α are presented in figure 9(a) for model 1 and in figure 9(b) for model 2. Similar plots of C_Y against β are presented in figure 10(a) for model 1 and in figure 10(b) for model 2. Summary plots showing C_{N_α} and C_{Y_β} against Mach number are presented in figure 11(a) for model 1 and in figure 11(b) for model 2. Theoretical values for C_{N_α} or $-C_{Y_\beta}$ as calculated from reference 1 (solid line curves) are also shown in figures 11(a) and 11(b). As may be seen in figure 11, the agreement between the experimental points of C_{N_α} and the theoretical curve is good for both models but the experimental points for $-C_{Y_\beta}$ are considerably higher than the theoretical values for both models. Since this result did occur on both models it is very unlikely that it is due to any instrument errors. It is believed that, if for some reason the vertical tails were in a more turbulent flow than the horizontal tails, the experimental values of C_{Y_β} would be less than theory rather than greater. It should be noted that the experimental values of C_{N_α} (or C_{Y_β}) are total derivatives, whereas the theoretical values of C_{N_α} presented are partial derivatives. Attempts were made to account for C_N due to $\dot{\theta}$ and C_Y due to $\dot{\psi}$ but no appreciable difference in the derivatives C_{N_α} and $-C_{Y_\beta}$ resulted. A somewhat similar phenomenon occurred during the test reported in reference 4 where C_{N_α} was the same for a model that rolled at about 5 radians per second as for a model that did not roll if the pitch controls were at a control deflection of 0°. However, if the pitch controls were deflected 5° and thus caused an asymmetry in the model, C_{N_α} was much greater for the model that rolled than for the model that did not roll. For any rocket-propelled model test, no exact evaluation of the asymmetries can be made since instrument mountings as well as lifting surfaces of the model are subject to construction tolerances. For both models of this report preflight measurements of wing misalinements showed them to be very small and about the same in the X,Y plane as in

the X,Z plane. This result is also indicated from the flight measurements of figure 6. Further investigation will be necessary if the causes of this large apparent asymmetry are to be completely understood.

Damping

The damping constant could not be reduced directly from the time history of α or C_N since the rather large roll rate caused the response to not be confined to the X,Z plane. Two of the methods used for reducing data from rolling symmetrical models are shown in references 5 and 6. Both methods involve the making of plots of C_N against C_Y or α against β and determining a resultant force coefficient. In this report the method of reference 5 was used primarily but the method of reference 6 was also used to check agreement. Sample plots of the variation of C_N with C_Y are shown in figure 12 for model 1 and figure 13 for model 2. These shapes are typical for a small value of the space-motion factor K which is described in reference 5. The value of $\frac{p}{\omega}$ for model 1 varied from -0.37 at M = 2.45 to -0.2 at M = 1.77. The value of $\frac{p}{\omega}$ for model 2 varied from -0.34 at M = 2.25 to -0.28 at M = 1.69. The plots of C_N against C_Y from all the pulses were very similar to figures 12 and 13 except for the first pulse of model 2. Inspection of the roll-rate trace in figure 7 shows that the second pulse rocket fired less than 0.1 second after the first pulse rocket finished firing. This model motion was somewhat similar to the motion resulting from one long burning pulse rocket and results in a very large value of the space-motion factor K. In fact, the model had rolled through more than 90° between the start of the first pulse rocket to burnout of the second pulse rocket. The plot of C_N against C_Y for these pulses, presented in figure 14, shows that the value of K is extremely large.

The time history of C_R^2 was obtained from the relationship $C_R^2 = \left(C_N - C_{N_t}\right)^2 + \left(C_Y - C_{Y_t}\right)^2$. A sample time history of C_R^2 as obtained from the plot of C_N against C_Y in figure 12 is shown in figure 15. The damping constant b as obtained from these time histories of C_R^2 is presented in figure 16. The damping constant b was also determined by using the method of reference 6, and these points are also included in figure 16. The excellent agreement between the values of b obtained by using the two methods is not surprising even with the large value of K for the first pulse of model 2. Close inspection of the two methods shows that, when the proper trim points are chosen, reference 6 does almost the same thing graphically as reference 5 does mathematically.

The damping derivative $C_{m_q} + C_{m_{\dot{\alpha}}}$ shown in figure 17 was determined from the damping constant b by using the relationship:

$$C_{m_q} + C_{m_{\dot{\alpha}}} = \left(- \frac{2I_Y}{qS\bar{c}} b + \frac{57.3\ C_{L_\alpha}\ I_Y}{mV\bar{c}} \right) \frac{2V}{\bar{c}}$$

The values of C_{L_α} used in this equation were the root-mean-square values of C_{N_α} and C_{Y_β}.

Also included in figure 17 are calculated values of $C_{m_q} + C_{m_{\dot{\alpha}}}$ obtained by using the method of reference 7. The fact that better agreement between theory and experiment is obtained for model 2 must be attributed to coincidence. The theoretical $C_{m_q} + C_{m_{\dot{\alpha}}}$ for model 2 was, of course, obtained by adding the effect of the forward surface and its downwash to the calculated values for model 1; therefore, the theory must have overestimated the contribution of the forward surface.

Pitching Moment

The static stability derivative C_{m_α} was obtained from the following relationship:

$$C_{m_\alpha} = - \frac{I_Y}{57.3qS\bar{c}} \left(\omega^2 + b^2 \right) - \frac{C_{L_\alpha}\ C_{m_q}\ \frac{\bar{c}}{2V}\ qS\bar{c}}{mV\bar{c}}$$

This is the equation for a nonrolling model. However equation (14) of reference 5 for a rolling model reduces to this equation if the magnus term is assumed to be negligible and I_X/I_Y is assumed to be zero. The quantity ω was determined from the period of the time history of $C_R{}^2$. Since the period of $C_R{}^2$ is one-half that of C_R, $\omega = \pi/\text{Period}$. The second term of the equation for C_{m_α} which is the contribution of the vertical translational degree of freedom was extremely small (less than 1 percent) for these heavy models having small lifting surfaces far away from the center of gravity. A plot of C_{m_α} against Mach number for both models is shown in figure 18. The aerodynamic center, as obtained from figure 18 and the root-mean-square values of C_{N_α} and $-C_{Y_\beta}$, is presented in figure 19. Also included in figure 19 are the aerodynamic-center positions as calculated from the theory of

reference 1. As in the case of the damping, the better agreement between theory and experiment in the case of model 2 must be attributed to coincidence.

Drag

The drag coefficient as a function of Mach number is presented in figure 20. Excellent agreement was obtained between C_D as determined from the CW Doppler radar unit and C_D as determined from the longitudinal accelerometer in the model. Since the angle of attack was always very small, it is essentially zero-lift drag. The angle-of-attack vane may have influenced the drag somewhat but its influence is believed to be small. In reference 6 when a slightly longer rod was used on the flow-direction indicator the drag obtained agreed well with that obtained from wind-tunnel tests. Reference 8 also indicates that, when a long rod is used, the reduction in nose drag is much less.

CONCLUDING REMARKS

An investigation has been conducted at high Reynolds number to see whether potential-flow theory will adequately predict the stability derivatives of a cruciform-missile configuration having an aspect-ratio-5 unswept tail and a fineness-ratio-20 blunt-nose body. One model also had cruciform, aspect-ratio-3.4, forward surfaces. The two models were given pitch disturbances while rolling at 5 to 10 radians per second. There appeared to be regions of separated flow on the bodies of both models flight tested above a Mach number of 1.9 even at angles of attack of less than 1°.

The slope of the variation of normal-force coefficient with angle of attack agreed very well with that obtained by theory for both models but the slope of the variation of side-force coefficient with angle of sideslip was much greater than that of normal-force coefficient or theory for both models. The cause of this additional side force is at present unknown.

The damping derivative of the model without forward surfaces was greater than that predicted by theory but good agreement between theory and experiment was obtained with the model having forward surfaces. This result indicates that in this case the theory overestimated the damping contribution of the forward surfaces.

The aerodynamic center of the model with no forward surfaces was much farther forward than would be predicted by theory. The fact that

better agreement between theory and experiment was obtained for the model with forward surfaces also indicates that in this case the theory overestimated the destabilizing effect of the forward surfaces.

Langley Aeronautical Laboratory,
National Advisory Committee for Aeronautics,
Langley Field, Va., January 11, 1957.

REFERENCES

1. Nielsen, Jack N., Kaattari, George E., and Anastasio, Robert F.: A Method for Calculating the Lift and Center of Pressure of Wing-Body-Tail Combinations at Subsonic, Transonic, and Supersonic Speeds. NACA RM A53G08, 1953.

2. Tucker, Warren A.: A Method for Estimating the Components of Lift of Wing-Body Combinations at Supersonic Speeds. NACA RM L52D22, 1952.

3. Mason, Homer P., and Gardner, William N.: A Limited Correlation of Atmospheric Sounding Data and Turbulence Experienced by Rocket-Powered Models. NACA TN 3953, 1957.

4. Lundstrom, Reginald R., and Baber, Hal T., Jr.: Some Effects of Roll Rate on the Longitudinal Stability Characteristics of a Cruciform Missile Configuration As Determined From Flight Test for a Mach Number Range of 1.1 to 1.8. NACA RM L55L16, 1956.

5. Nelson, Robert L.: The Motions of Rolling Symmetrical Missiles Referred to a Body-Axis System. NACA TN 3737, 1956.

6. Baber, Hal T., Jr., and Moul, Martin T.: Longitudinal Stability and Control Characteristics As Determined by Rocket-Model Technique for an Inline, Cruciform, Canard Missile Configuration with a Low-Aspect-Ratio Wing Having Trailing-Edge Flap Controls for a Mach Number Range of 0.7 to 1.8. NACA RM L54B12, 1955.

7. Gillis, Clarence L., and Chapman, Rowe, Jr.: Summary of Pitch-Damping Derivatives of Complete Airplane and Missile Configurations As Measured in Flight at Transonic and Supersonic Speeds. NACA RM L52K20, 1953.

8. Jones, Jim J.: Experimental Drag Coefficients of Round Noses With Conical Windshields at Mach Number 2.72. NACA RM L55E10, 1955.

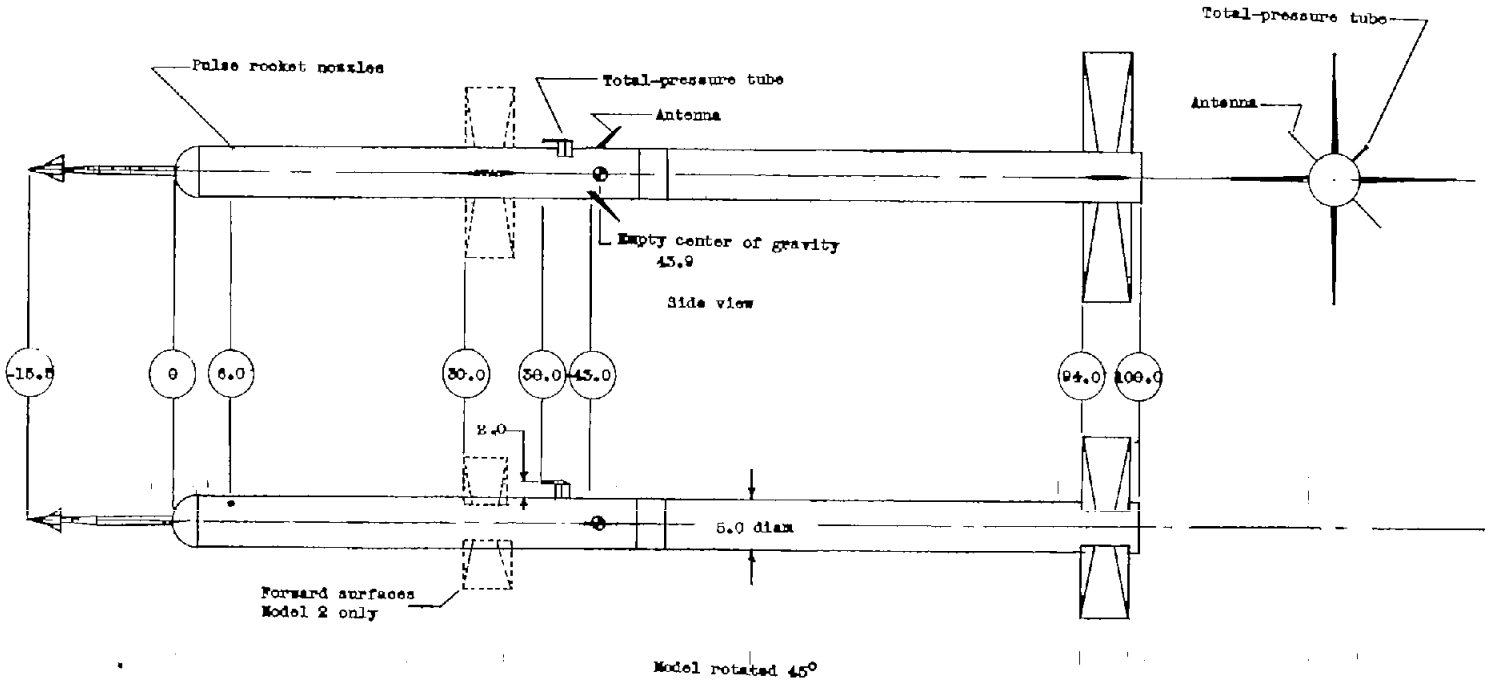

Figure 1.- Sketch of models tested. All dimensions are in inches.

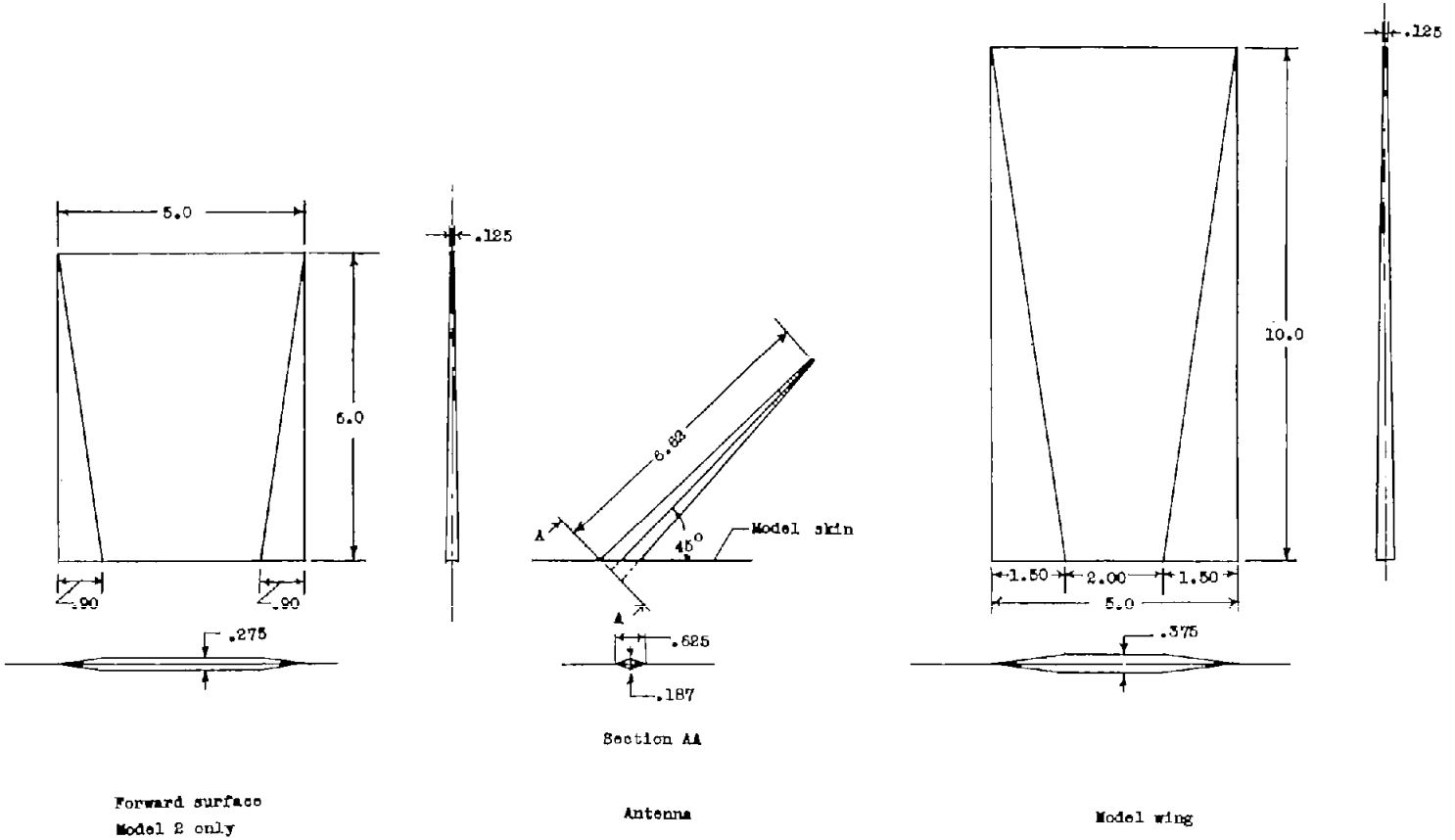

Figure 2.- Sketch of forward surface, antenna, and model wing for models tested. All dimensions are in inches.

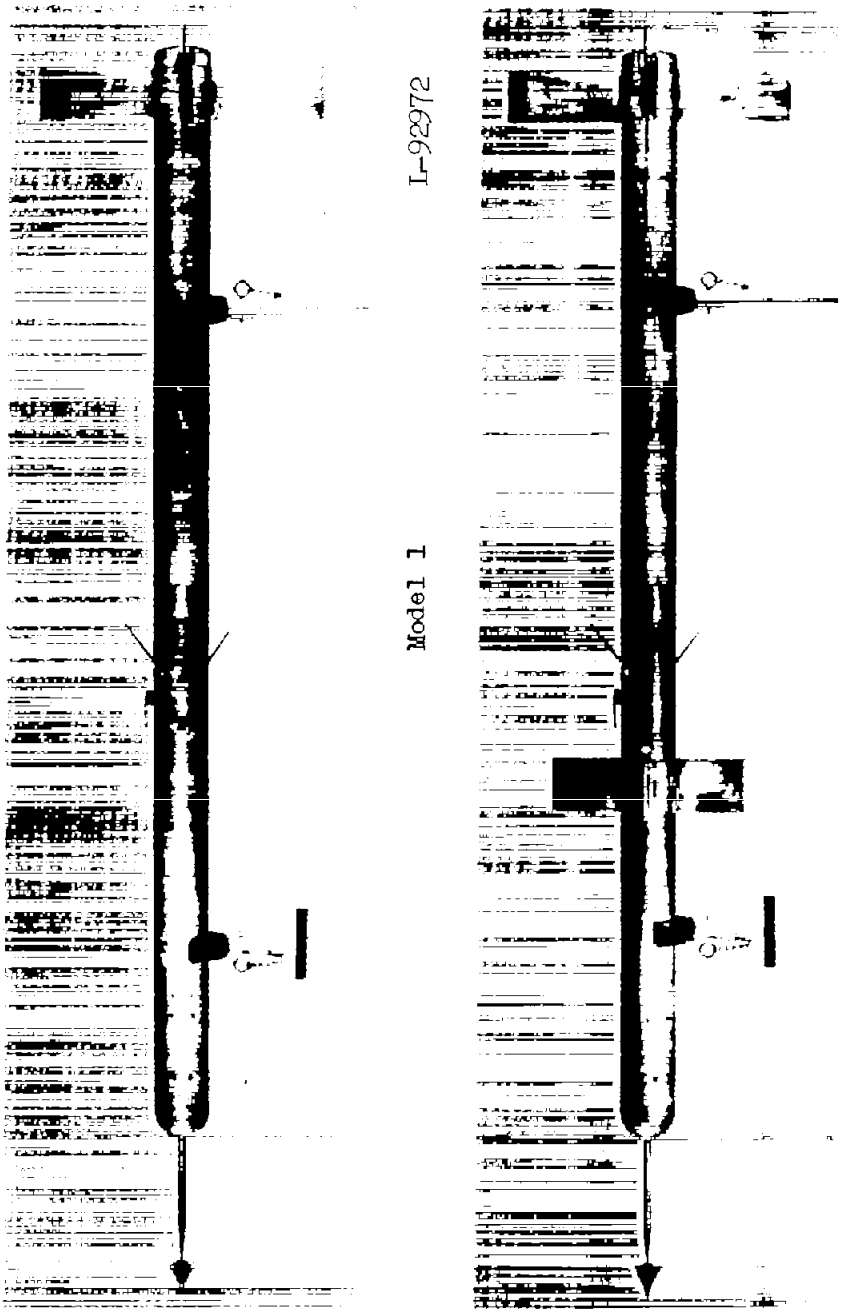

L-92972 Model 1 L-92973 Model 2

Figure 3.- Photographs of models tested.

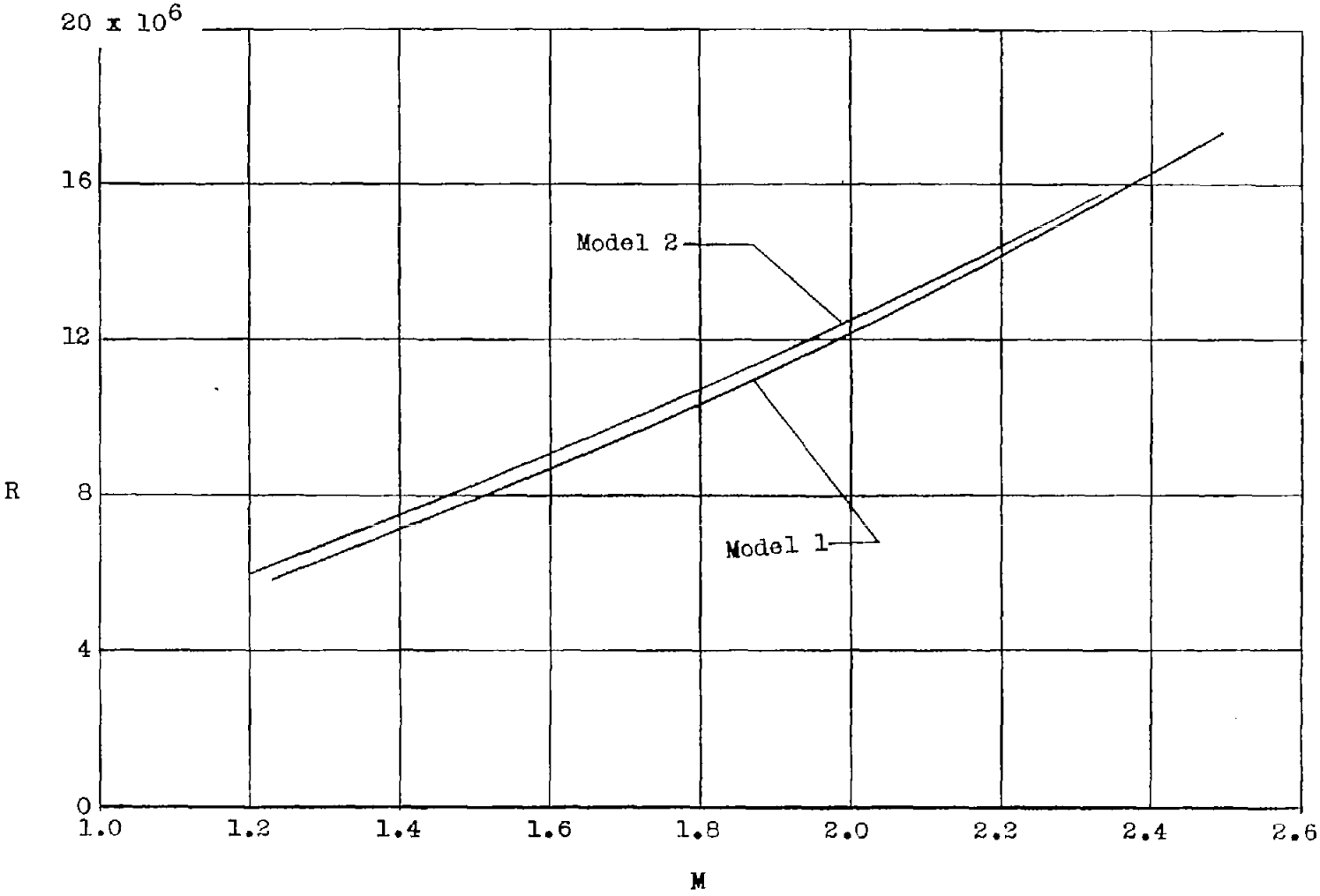

Figure 4.- Variation of Reynolds number per foot for models tested.

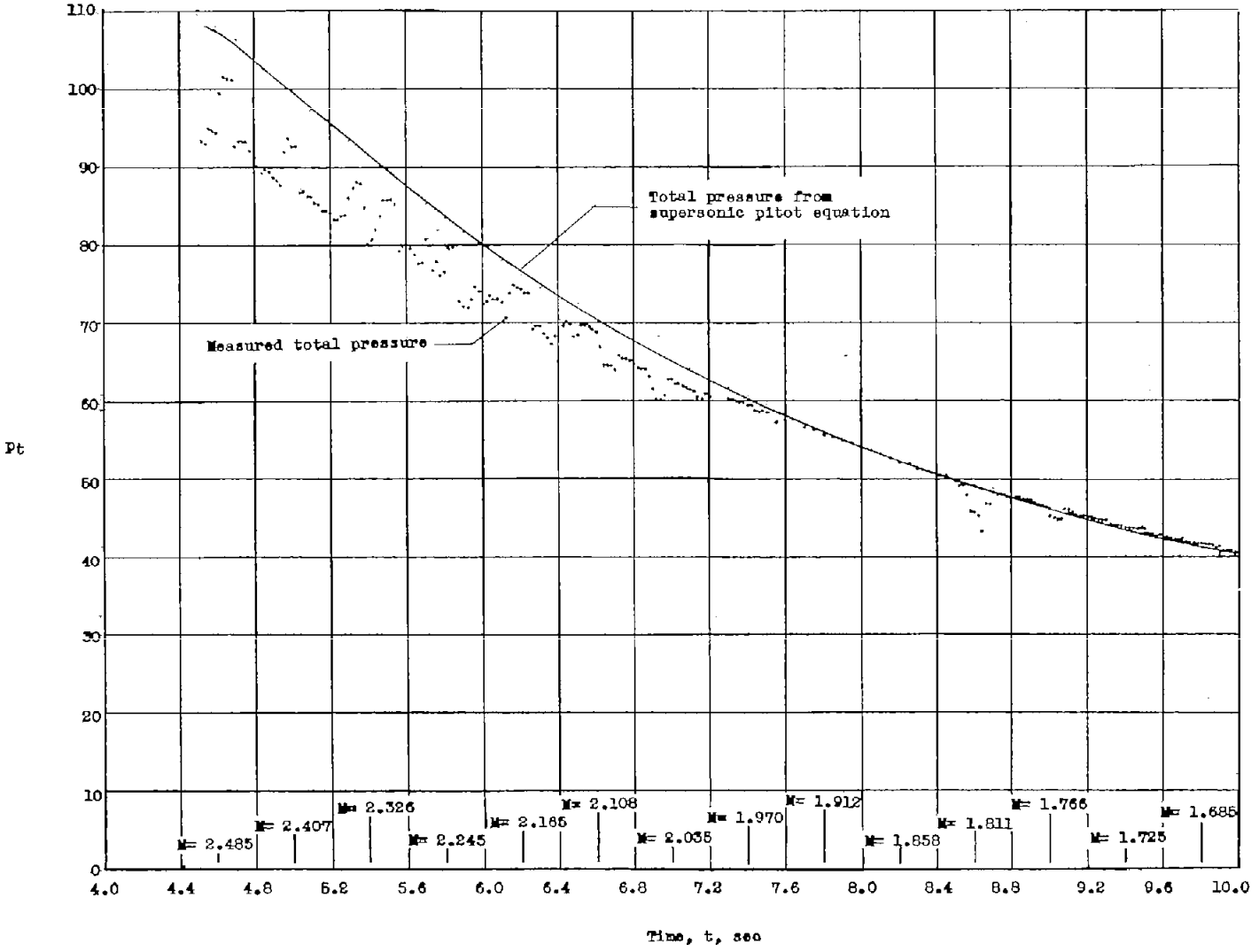

Figure 5.- Comparison of measured total pressure and calculated total pressure for model 1.

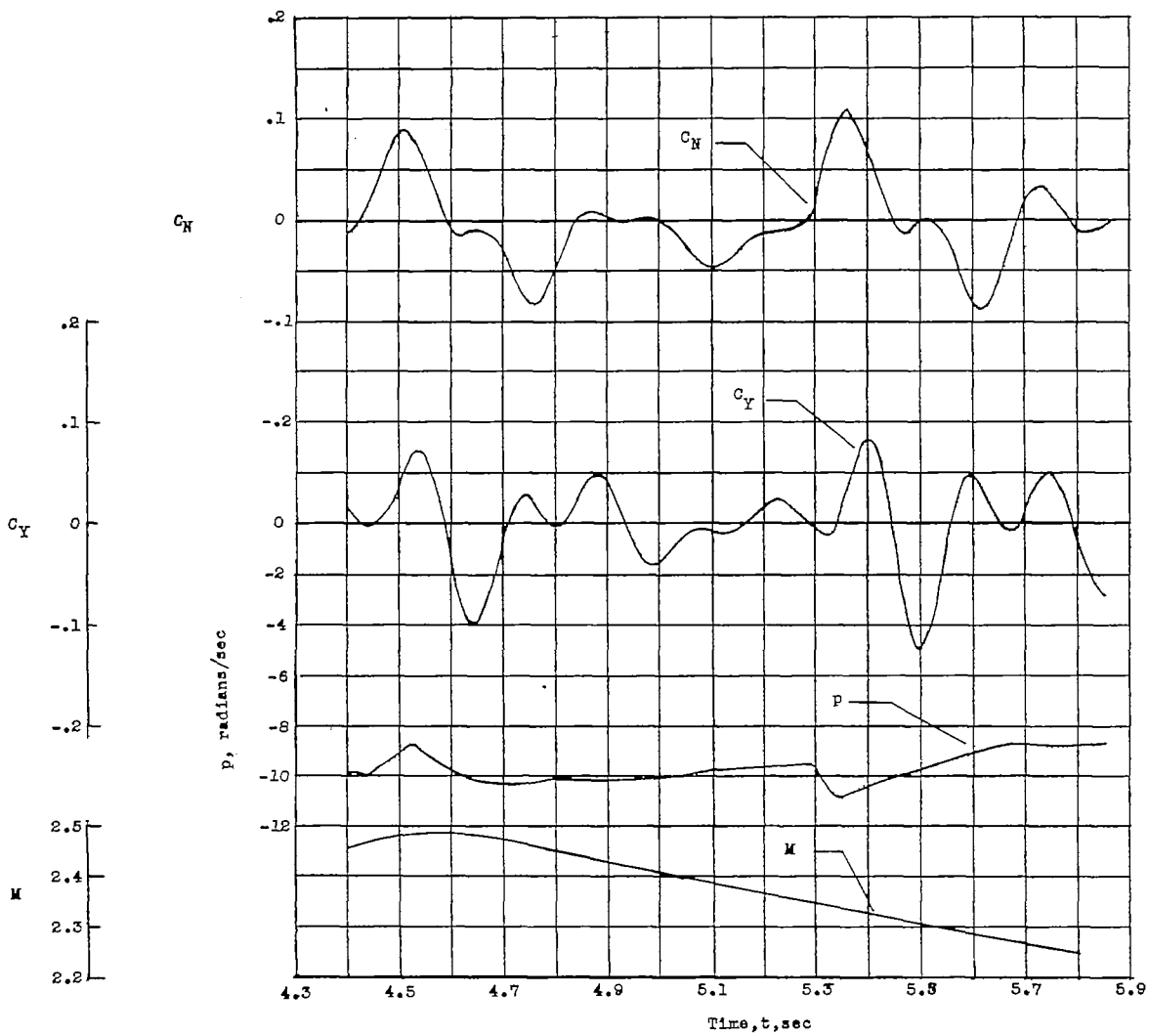

Figure 6.- Time histories of C_N, C_Y, p, and M for model 1.

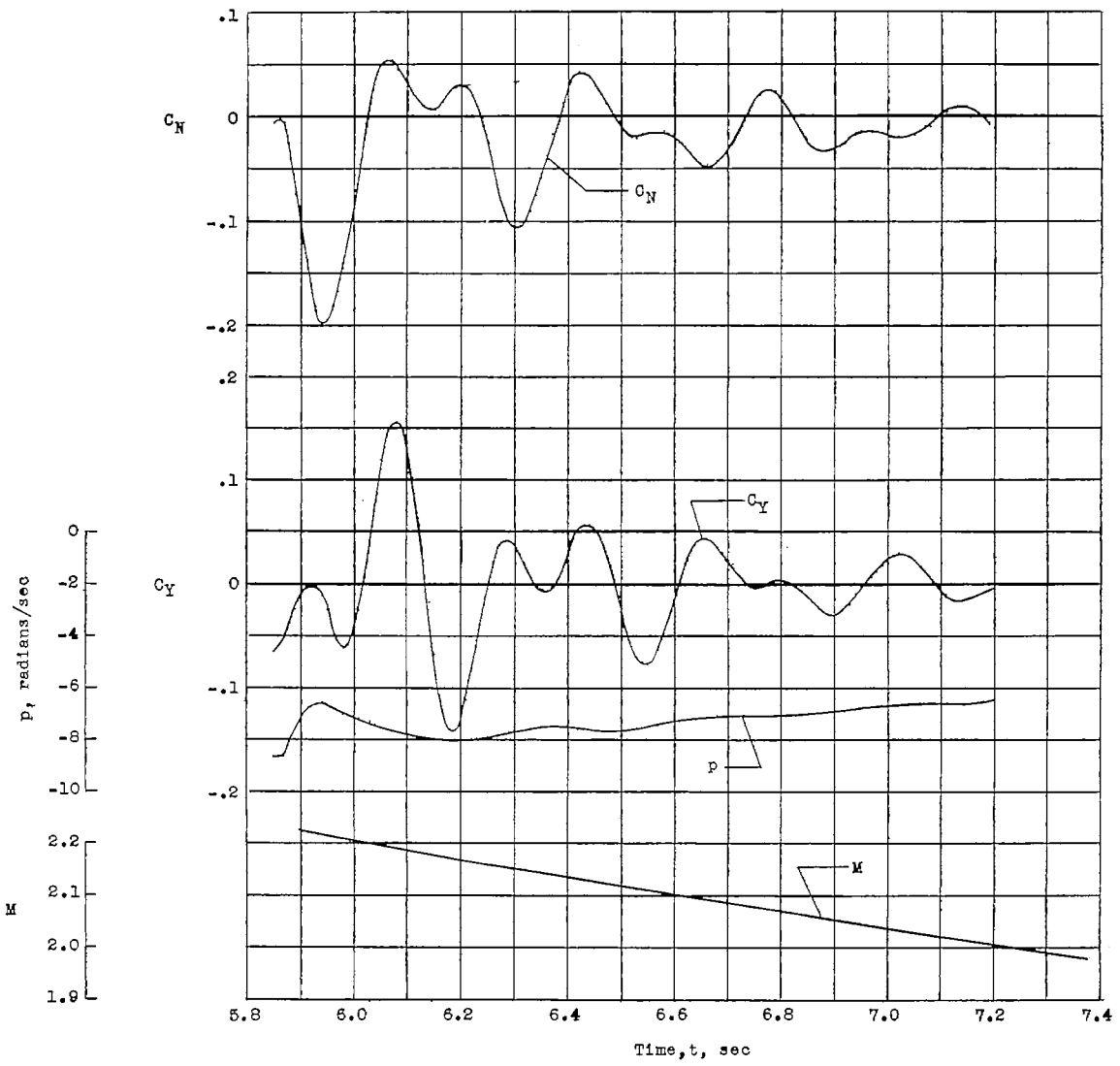

Figure 6.- Continued.

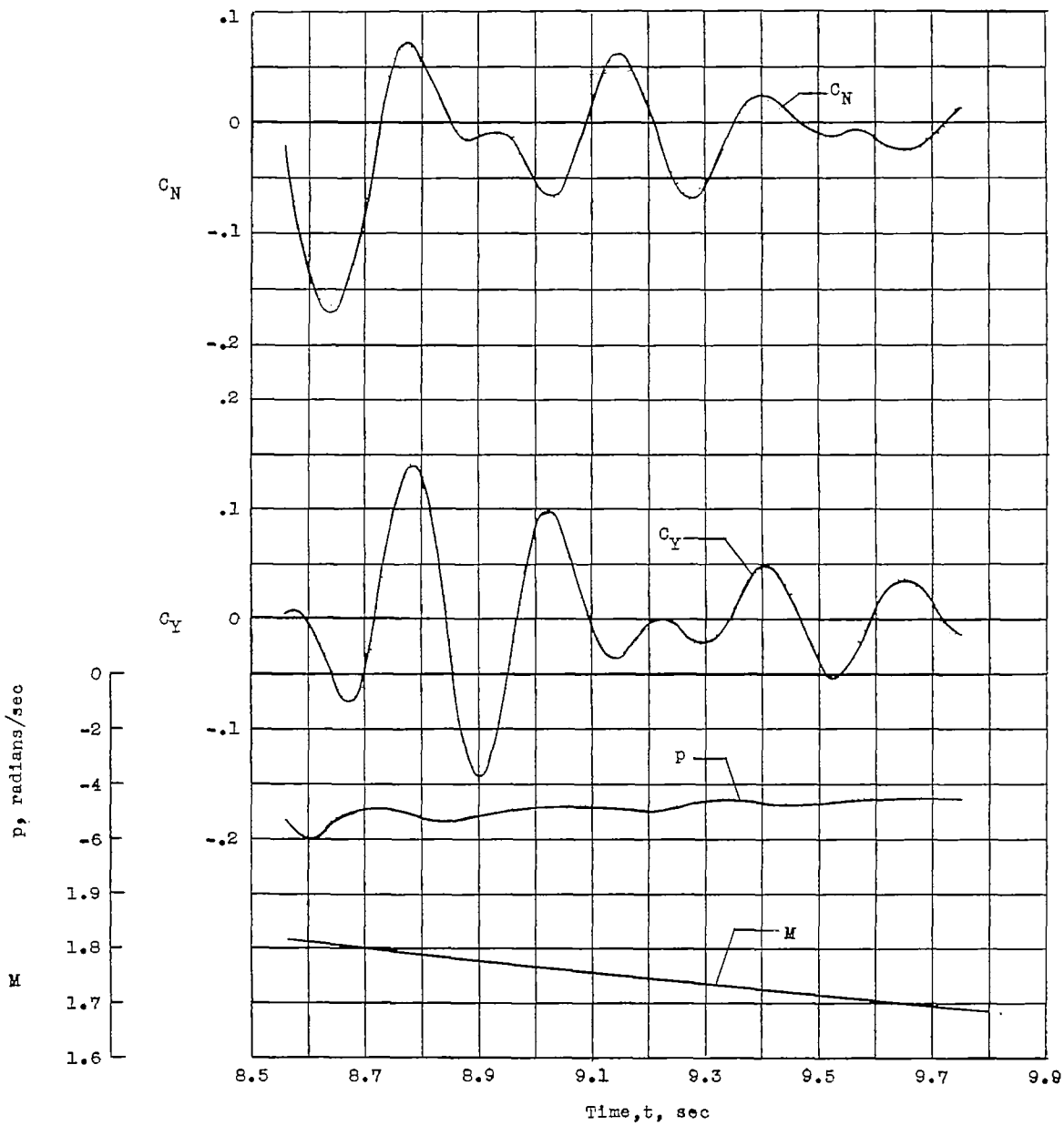

Figure 6.- Concluded.

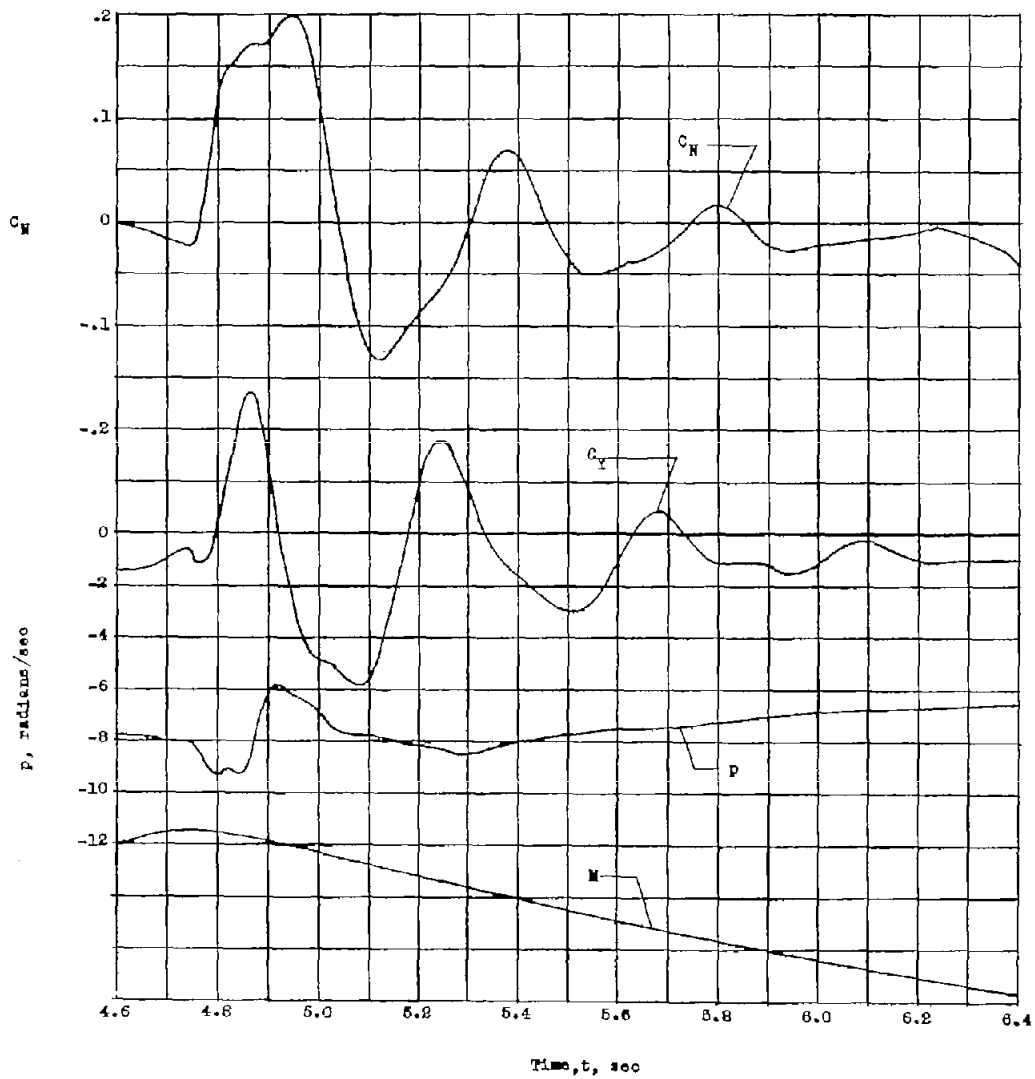

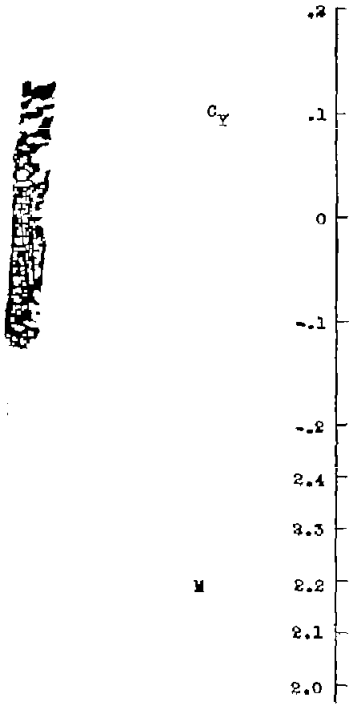

Figure 7.- Time histories of C_N, C_Y, p, and M for model 2.

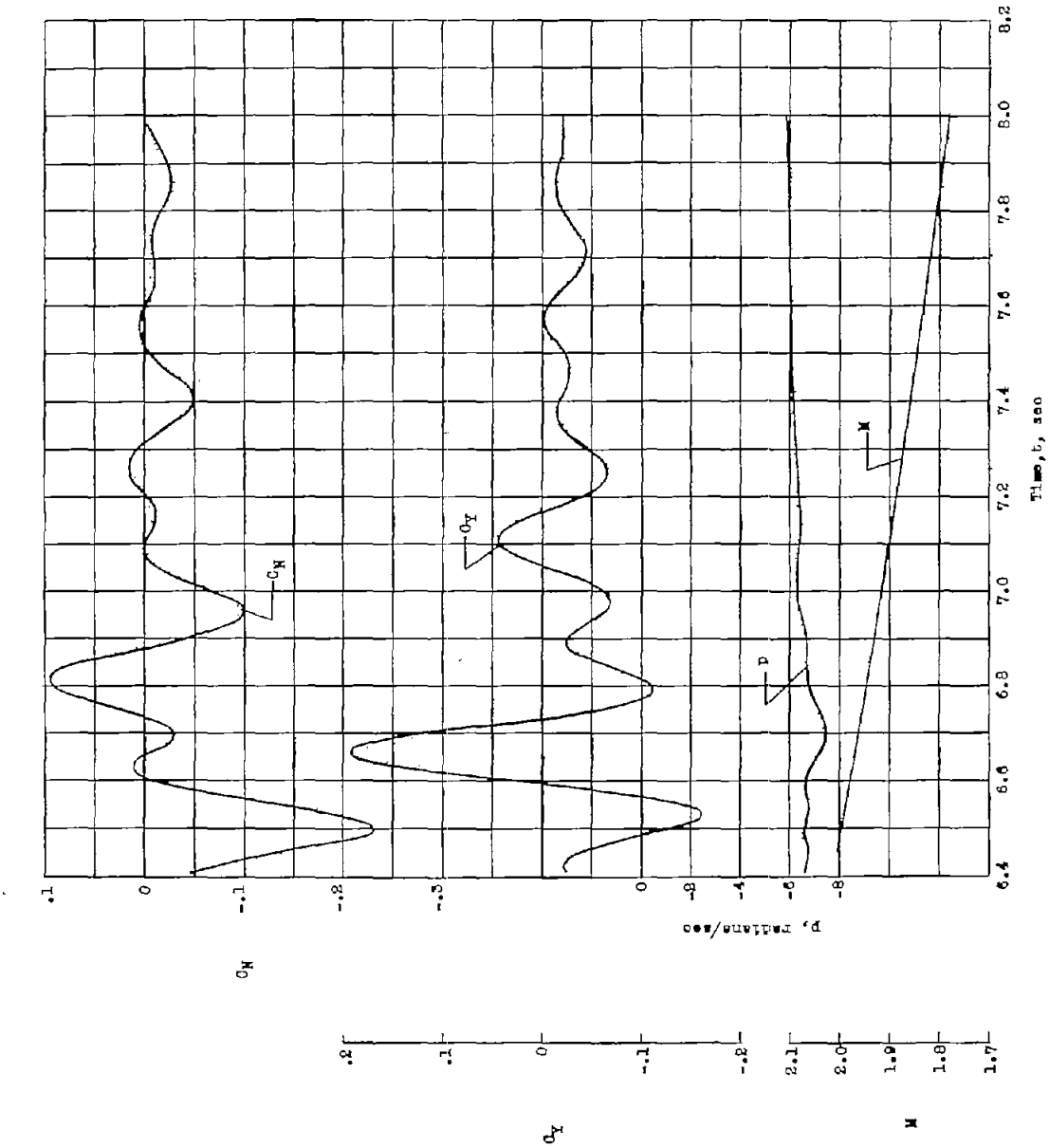

Figure 7.- Continued.

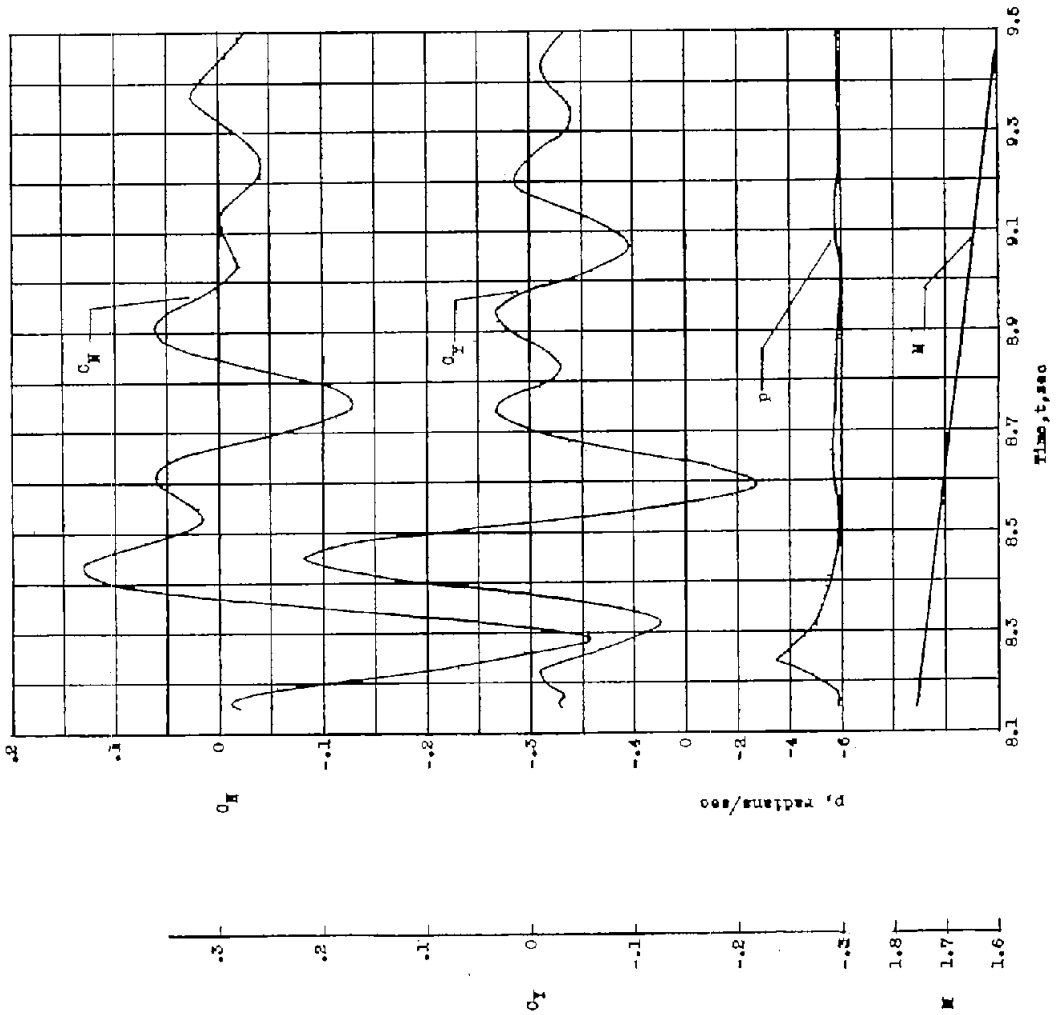

Figure 7.- Concluded.

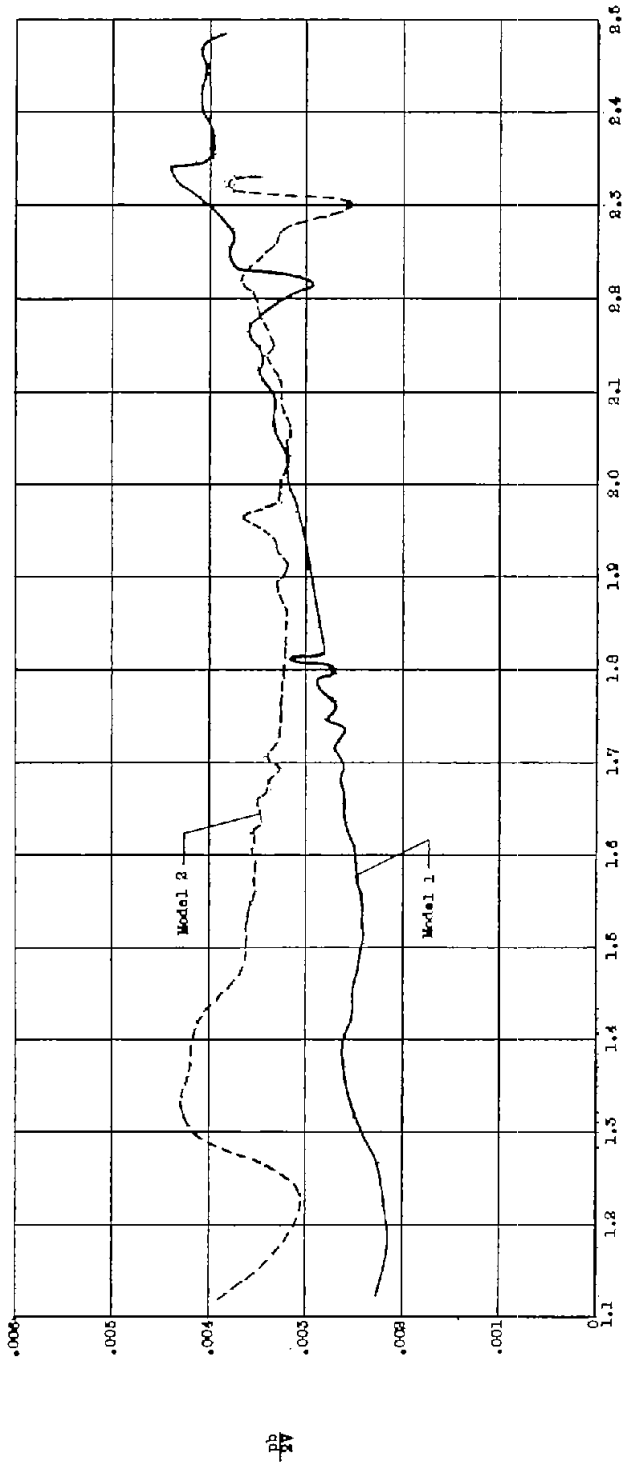

Figure 8.- Variation of wing-tip helix angle pb/2V with Mach number.

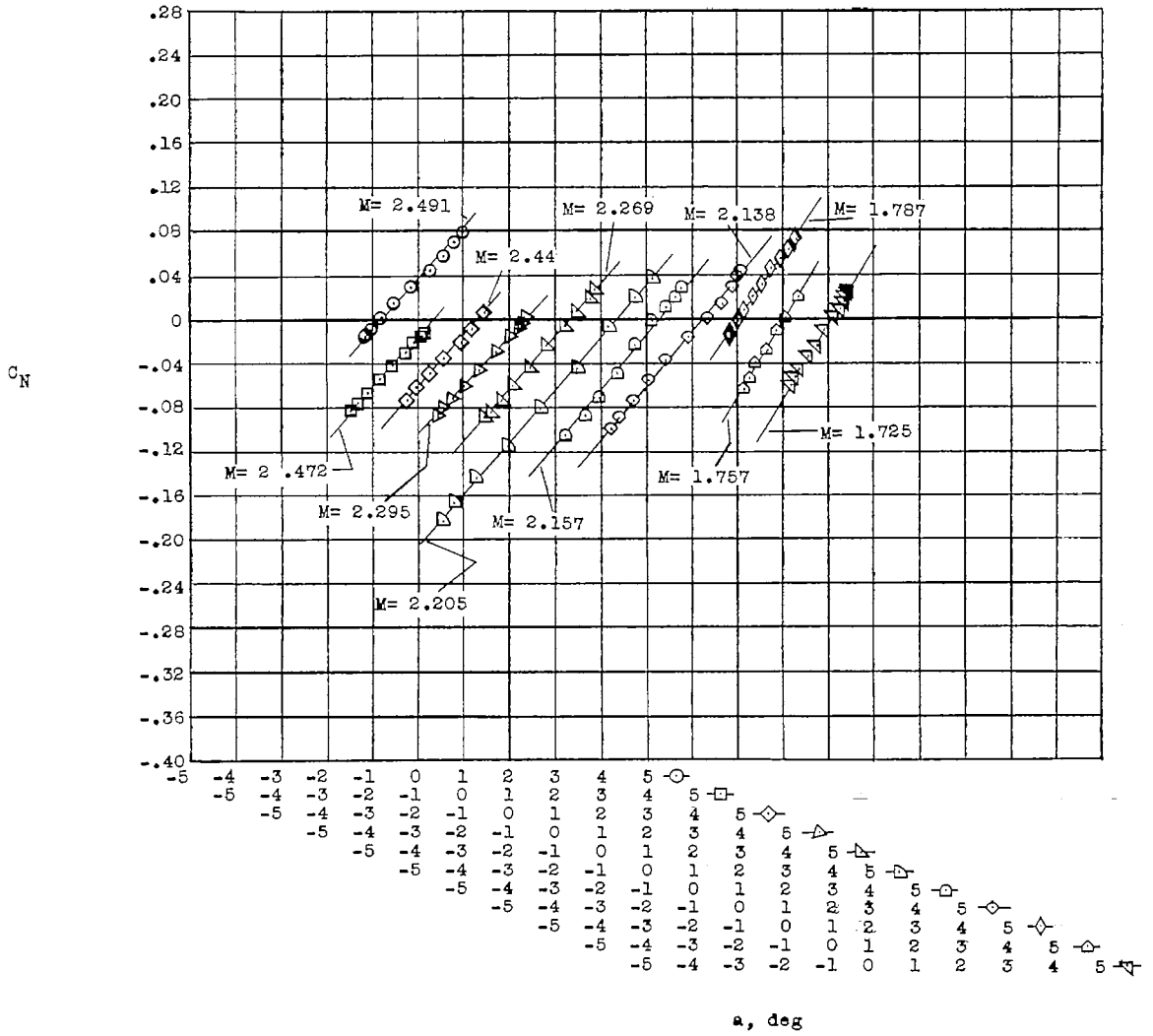

(a) Model 1.

Figure 9.- Variation of normal-force coefficient with angle of attack.

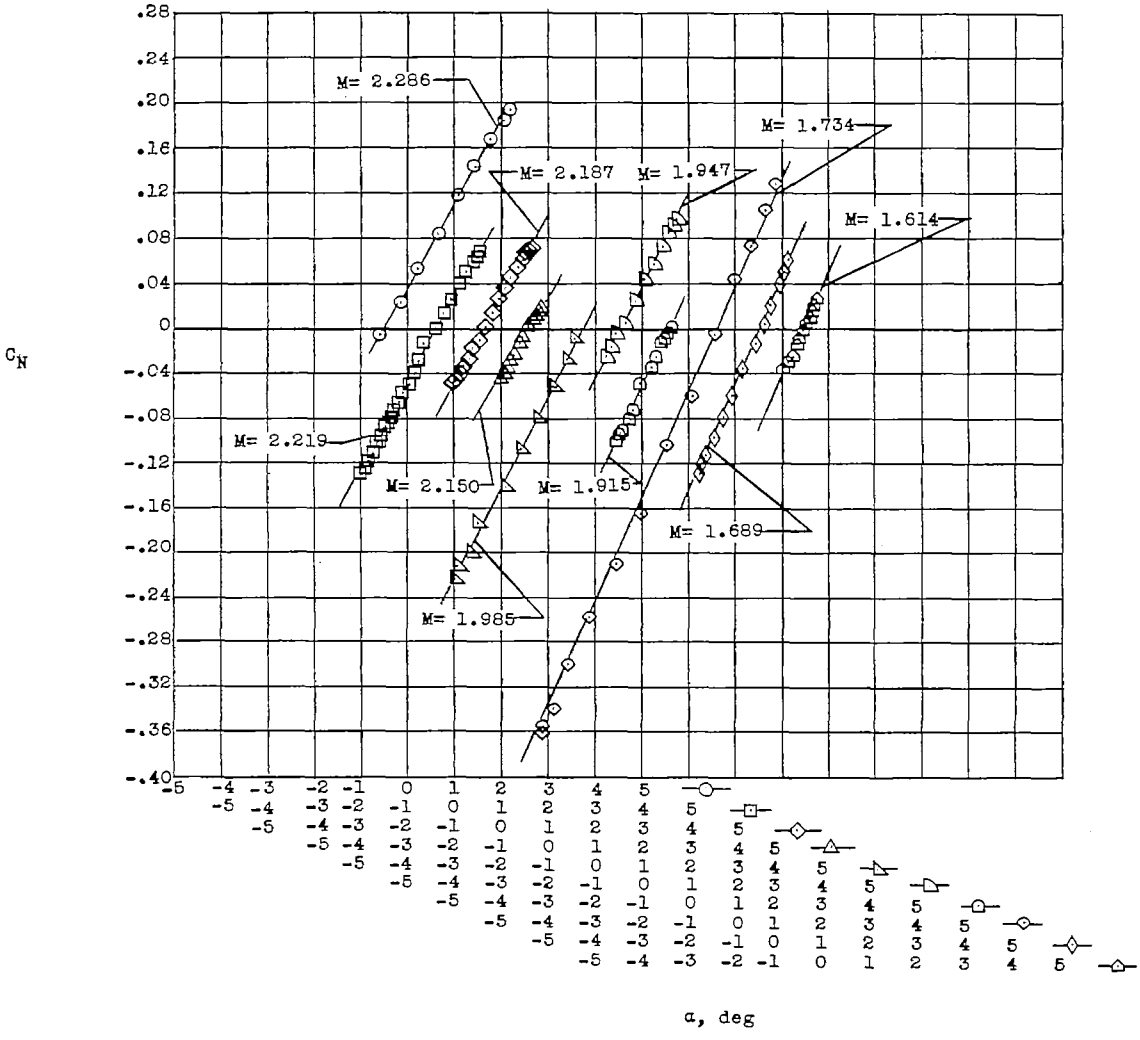

(b) Model 2.

Figure 9.- Concluded.

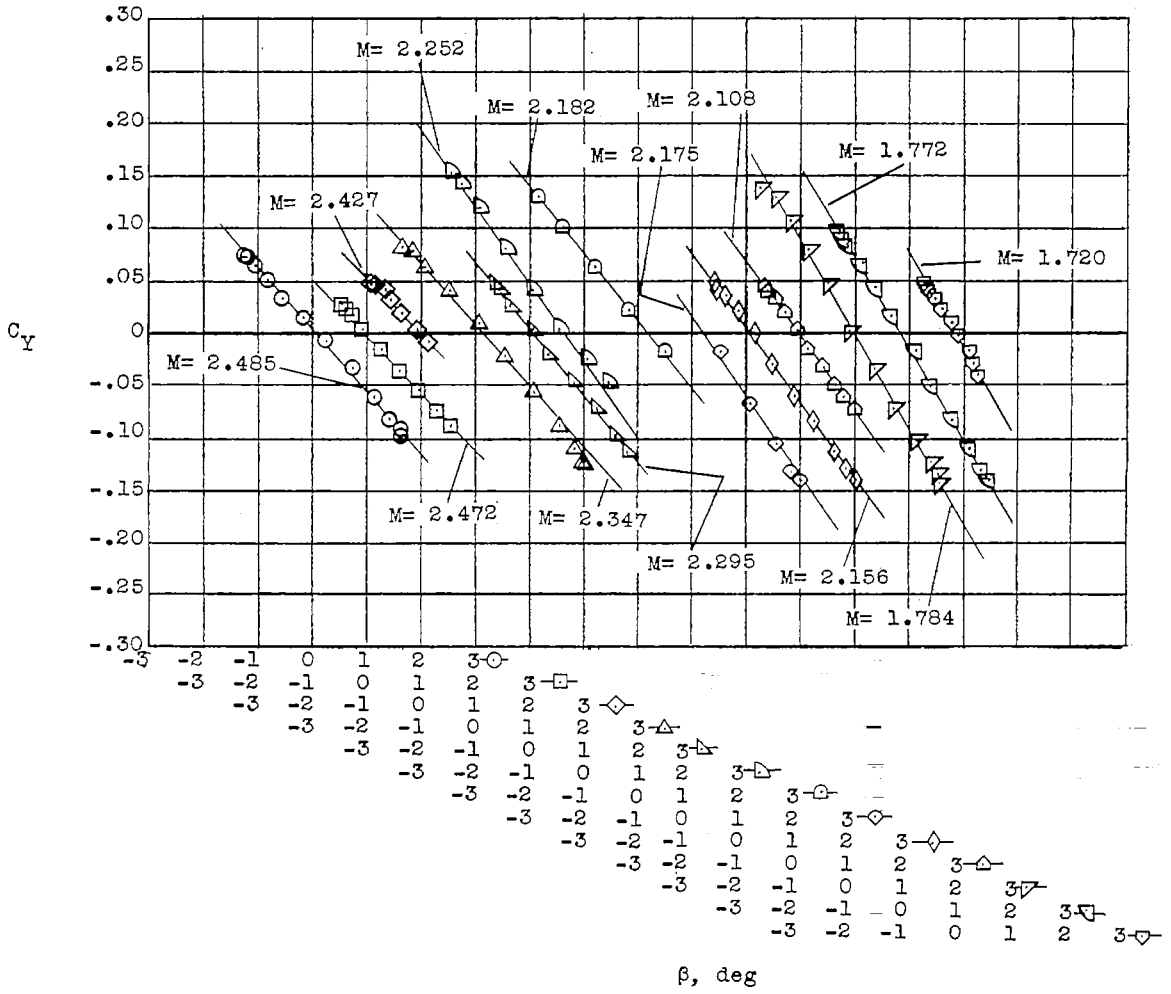

(a) Model 1.

Figure 10.- Variation of side-force coefficient with angle of sideslip.

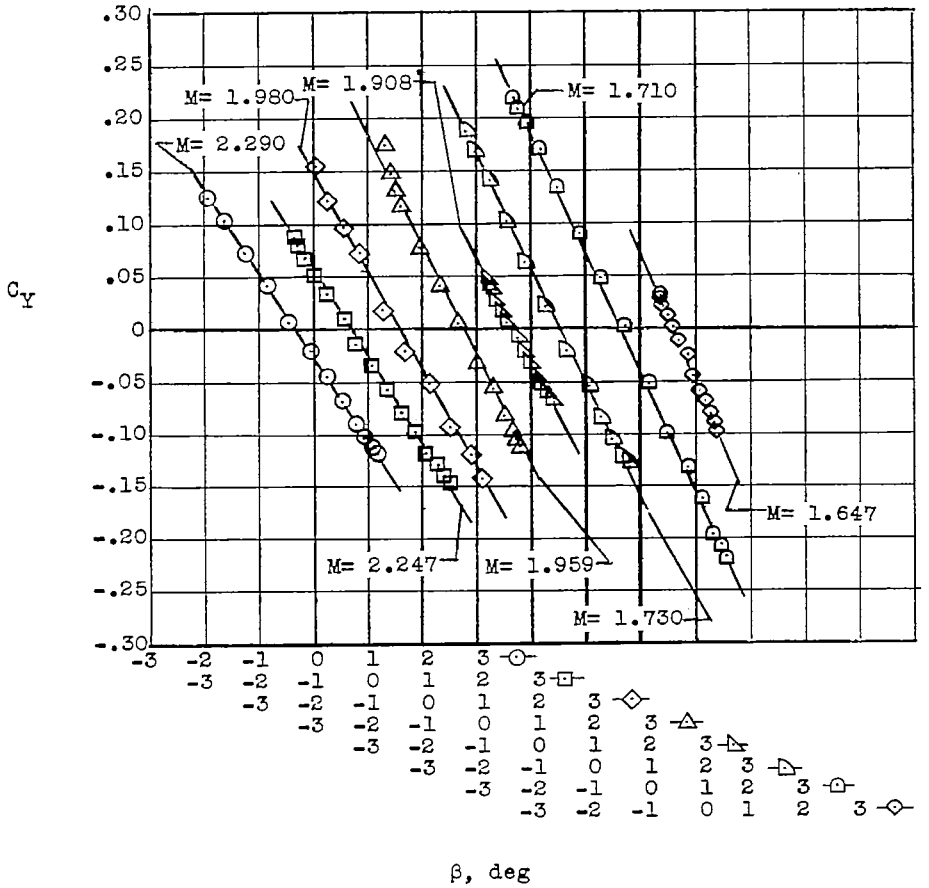

(b) Model 2.

Figure 10.- Concluded.

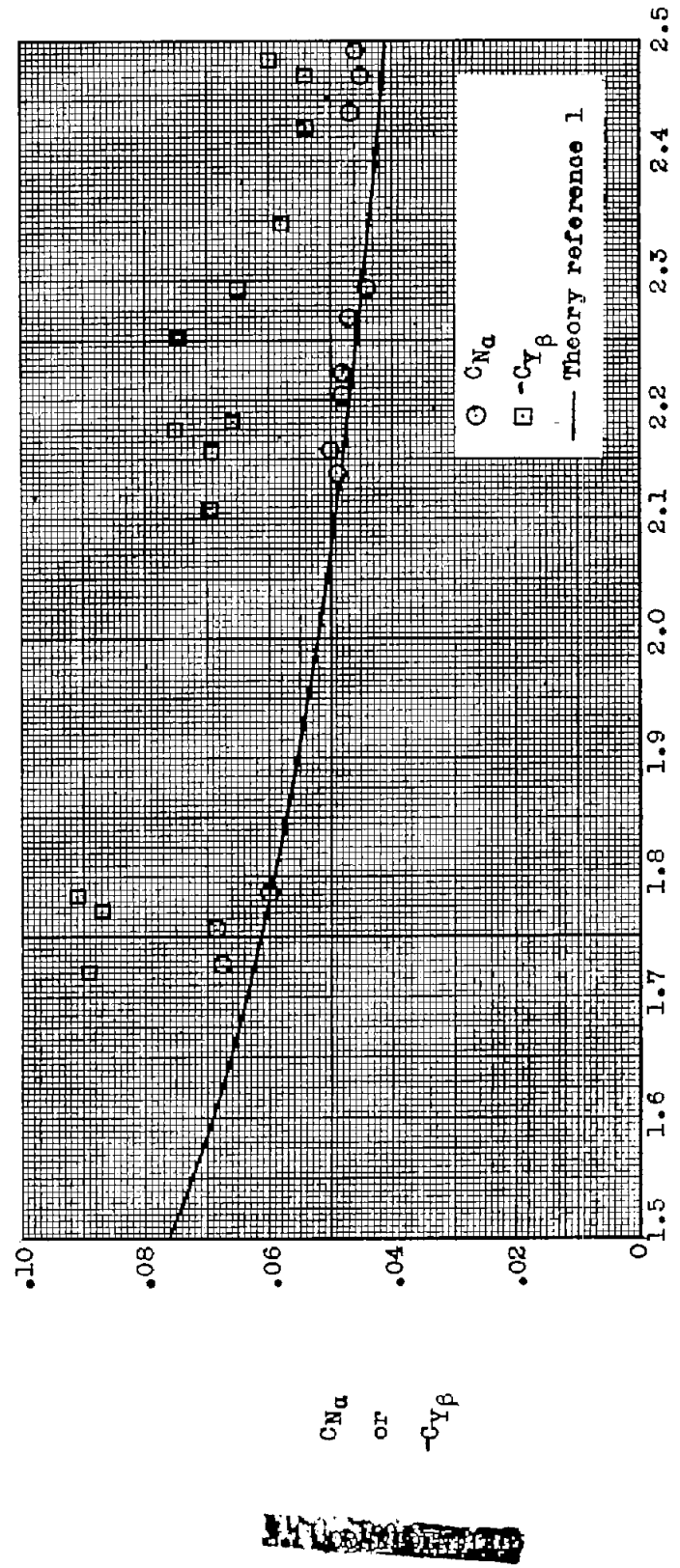

(a) Model 1.

Figure 11.- Variation of C_{N_α} and C_{Y_β} with Mach number.

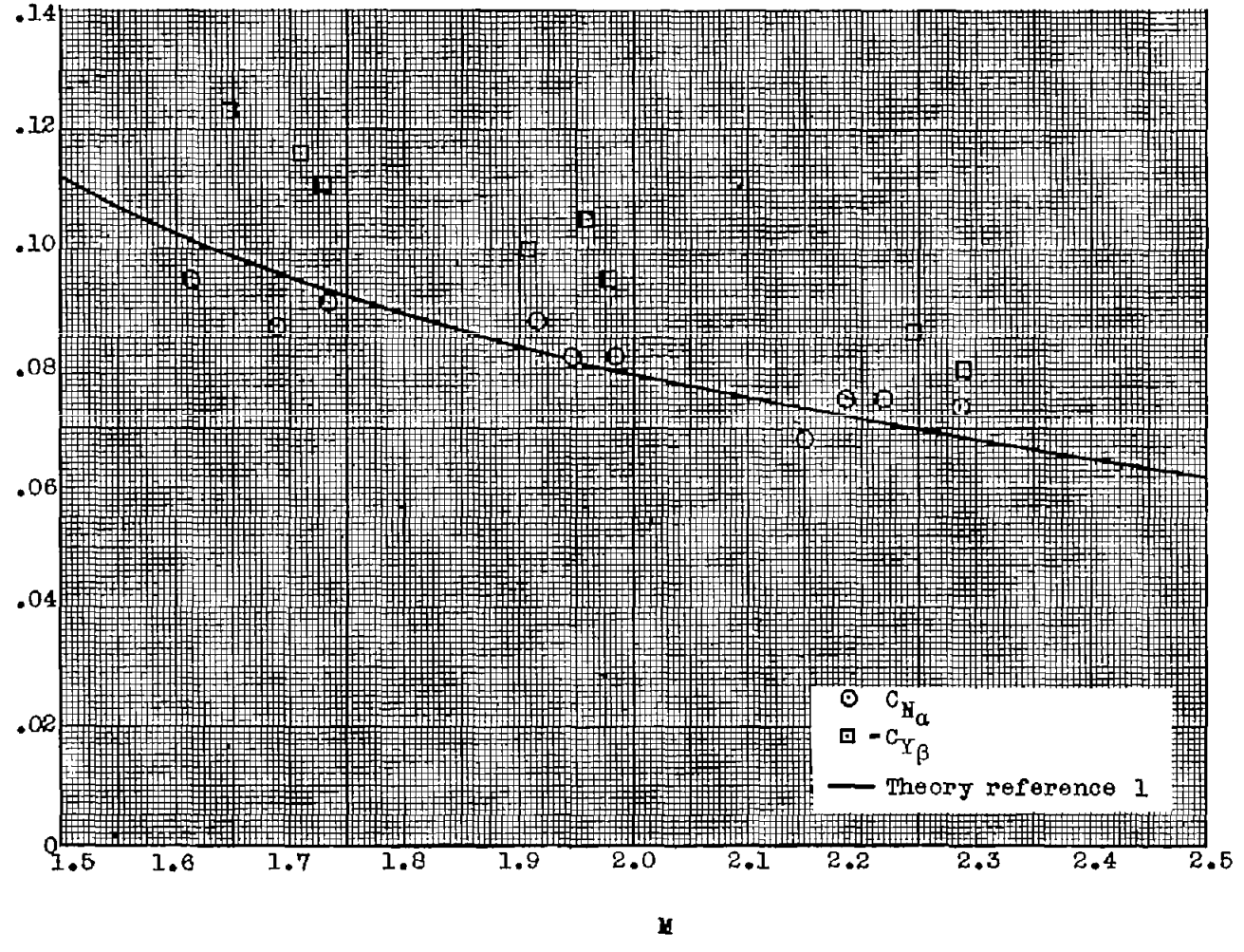

(b) Model 2.

Figure 11.- Concluded.

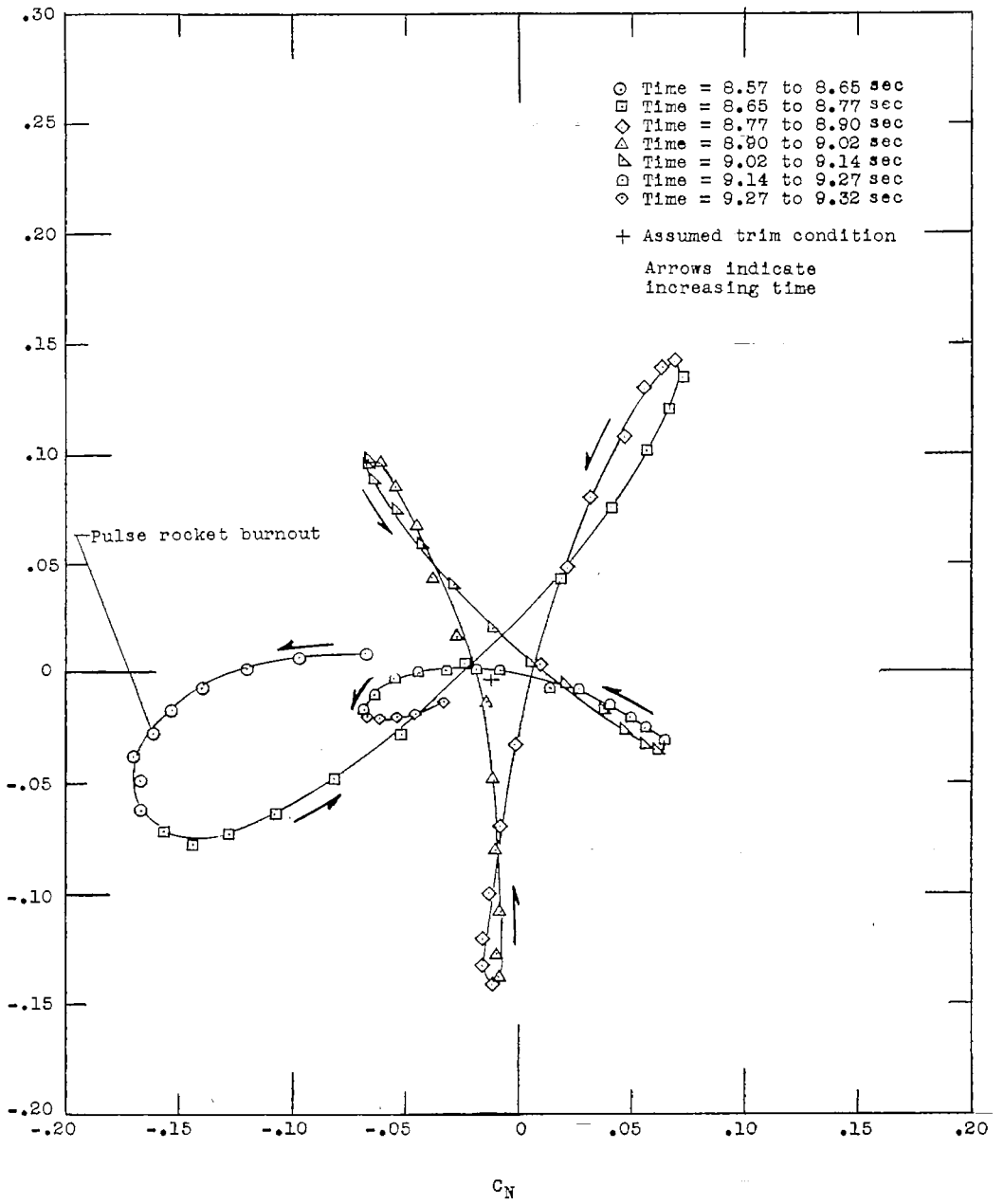

Figure 12.- Typical plot of C_N against C_Y for model 1.

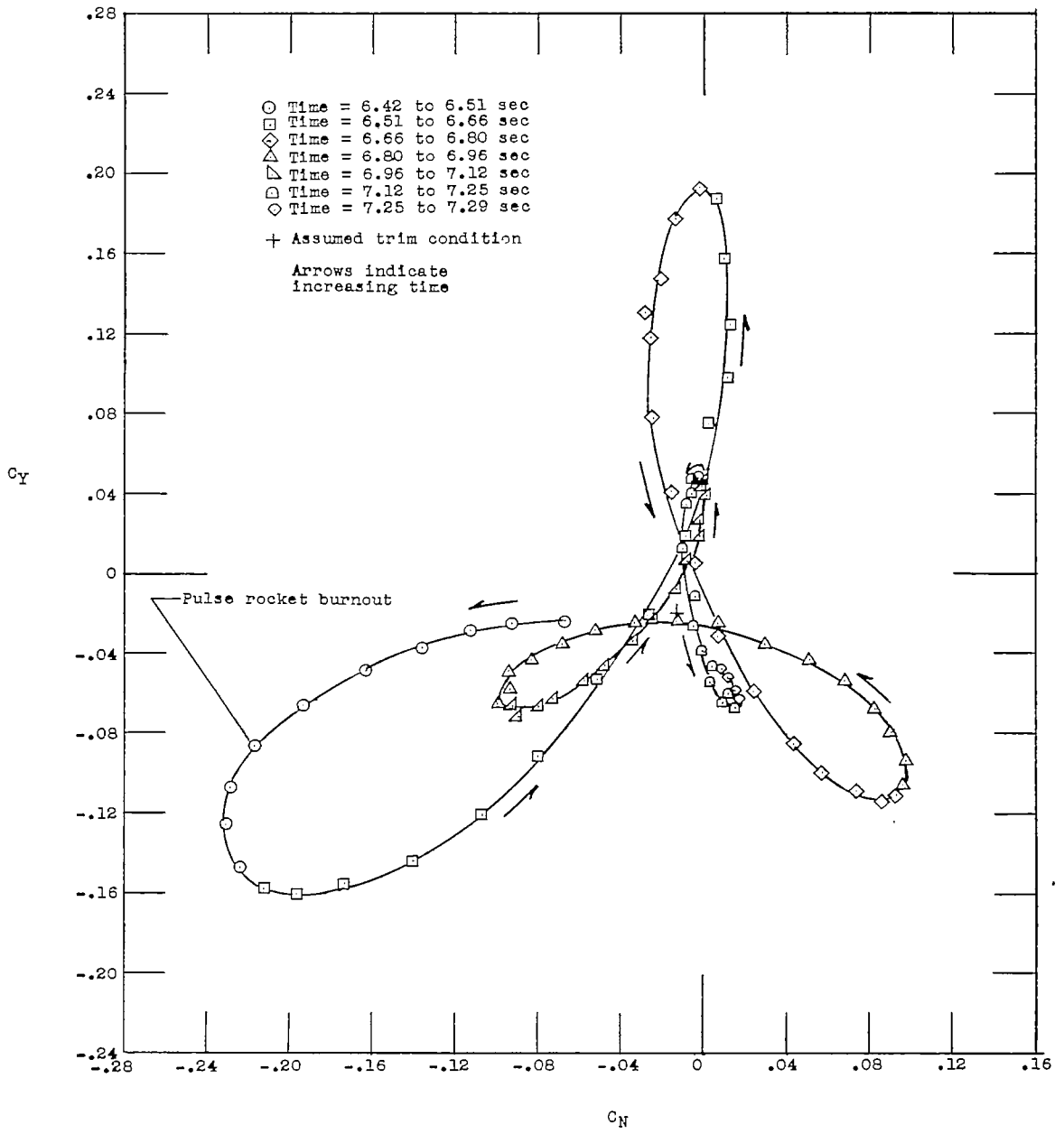

Figure 13.- Typical plot of C_N against C_Y for model 2.

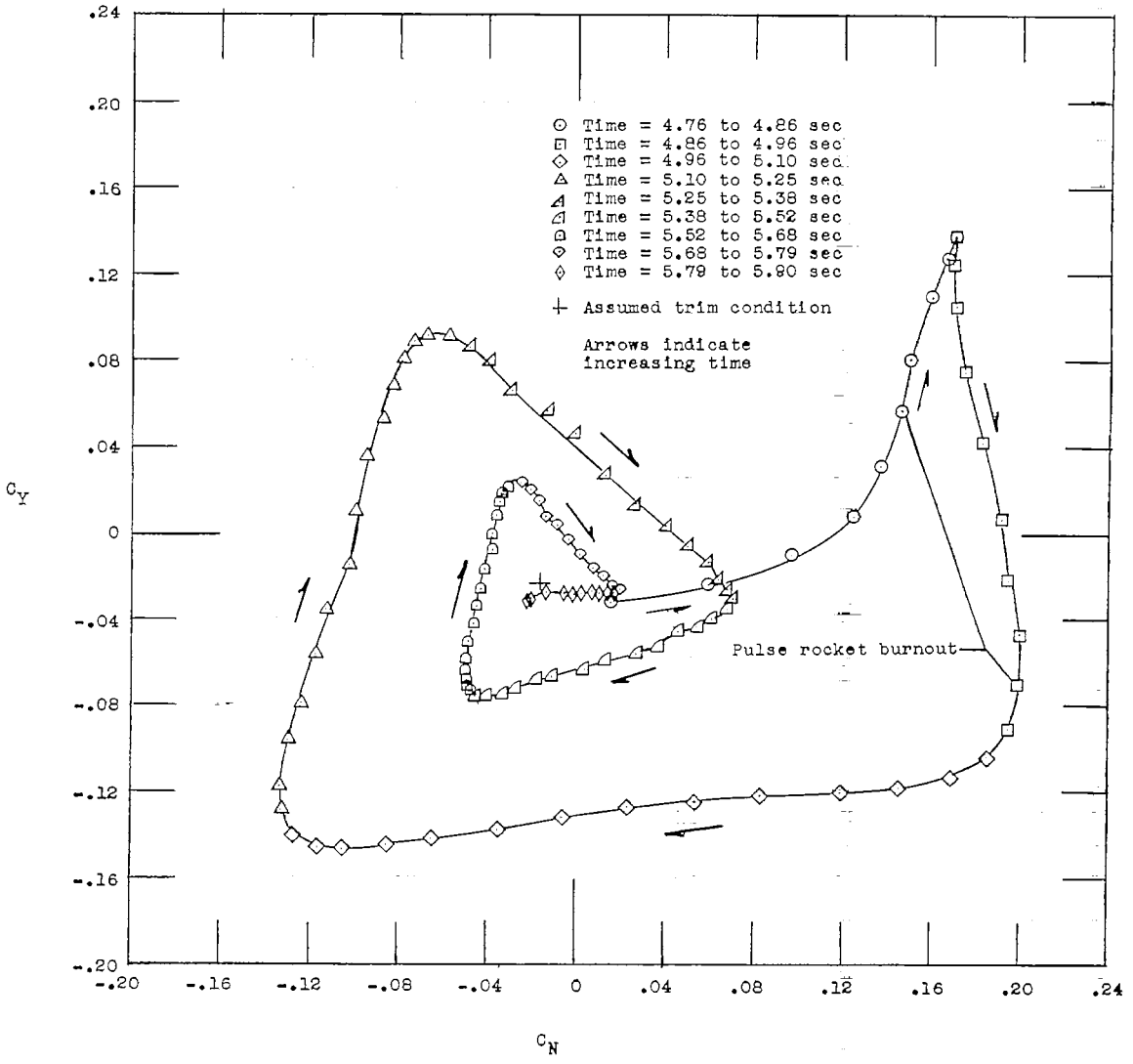

Figure 14.- Plot of C_N against C_Y for first two pulse rockets of model 2.

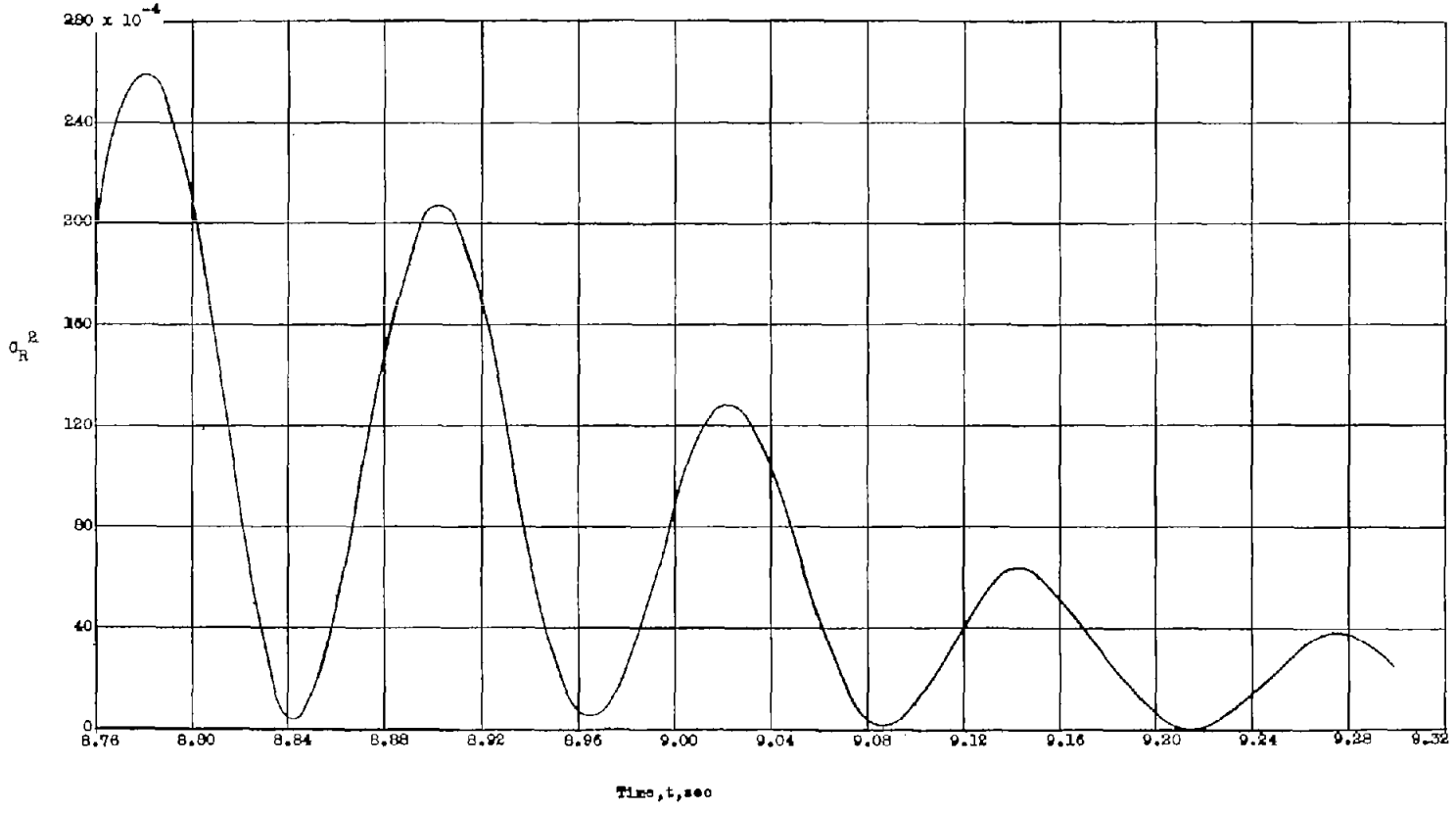

Figure 15.- Sample plot of C_R^2 with time.

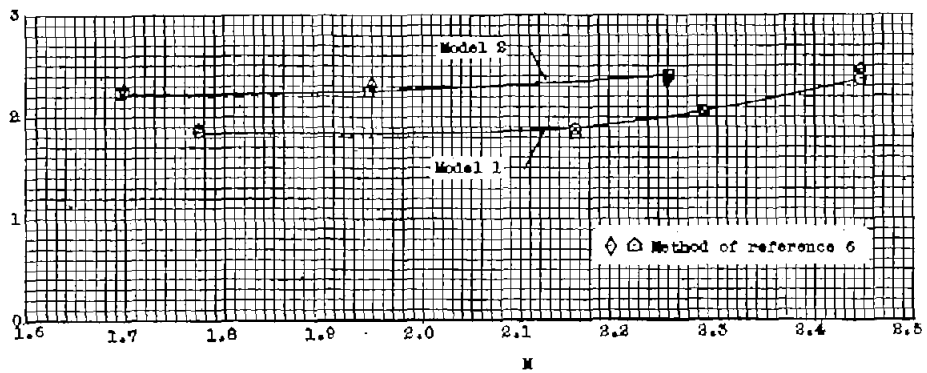

Figure 16.- Variation of the exponential damping constant b with Mach number for models 1 and 2.

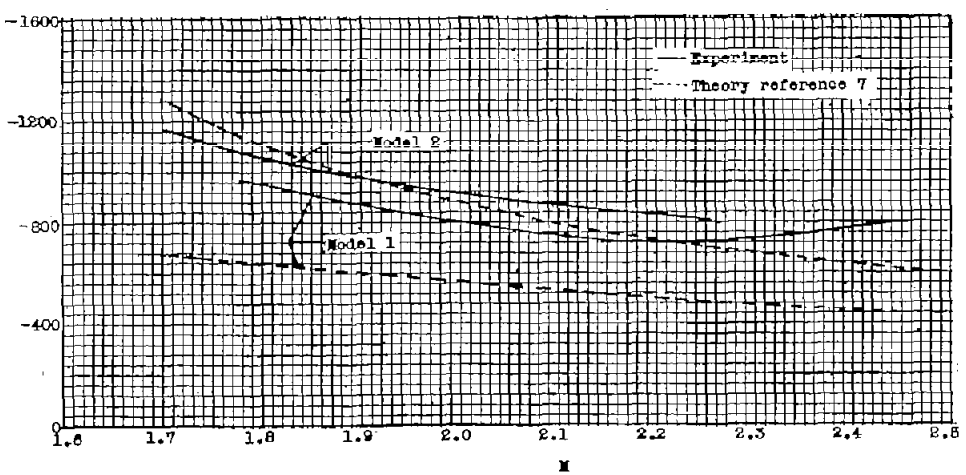

Figure 17.- Variation of the damping-in-pitch derivative $C_{m_q} + C_{m_{\dot{\alpha}}}$ with Mach number for models 1 and 2.

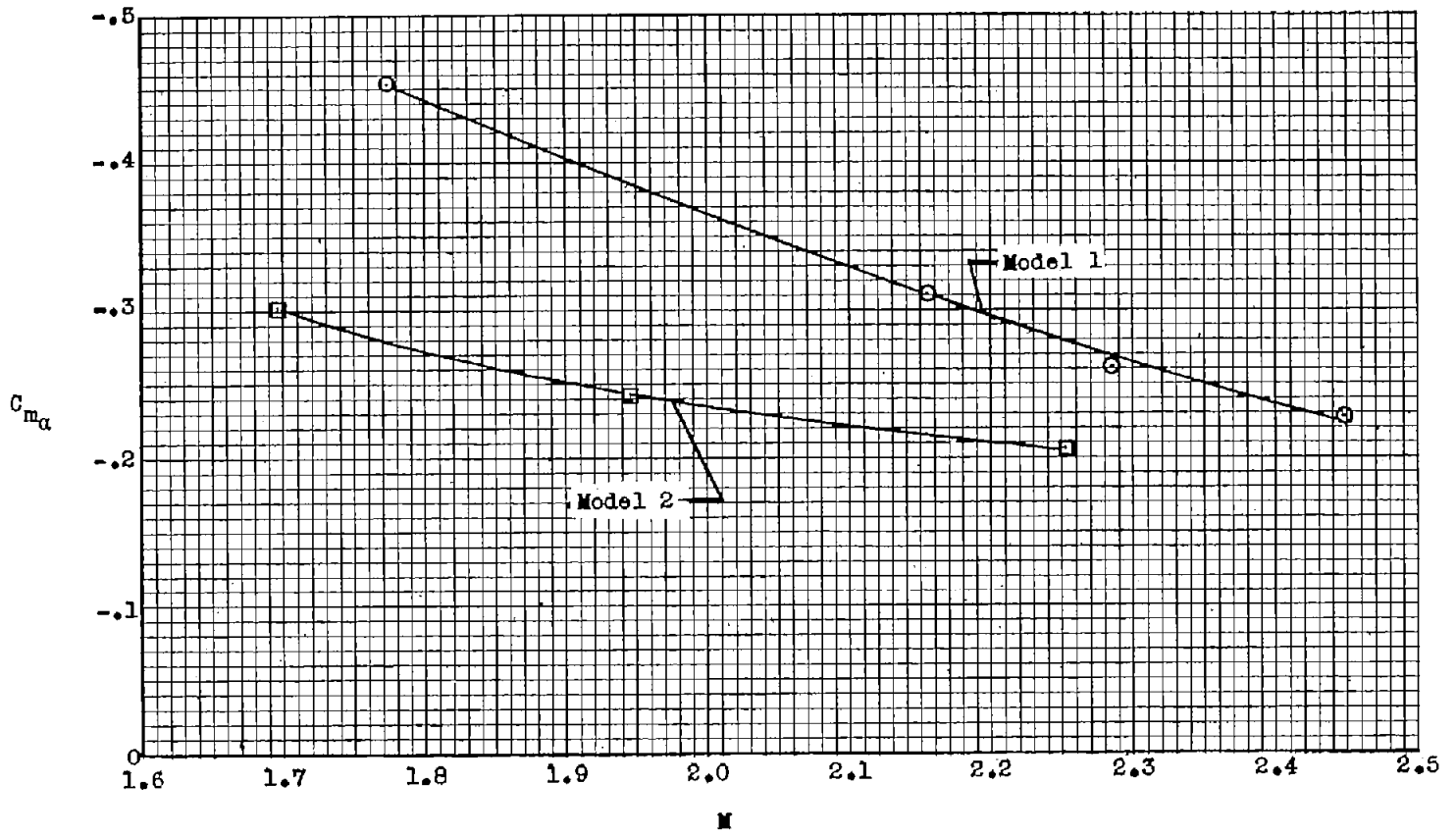

Figure 18.- Variation of the static stability derivative C_{m_α} with Mach number for models 1 and 2.

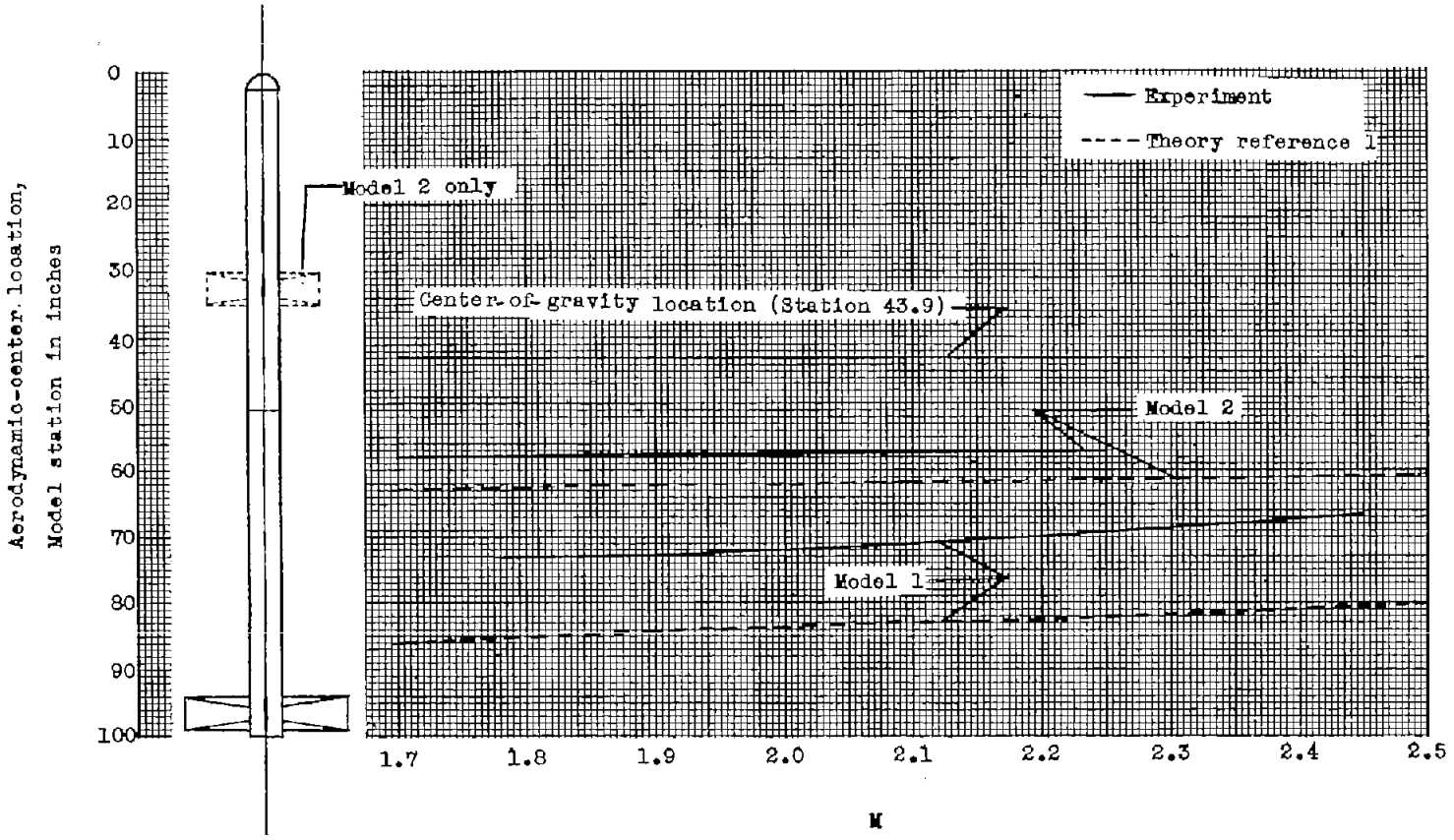

Figure 19.- Variation of the aerodynamic-center location with Mach number for models 1 and 2.

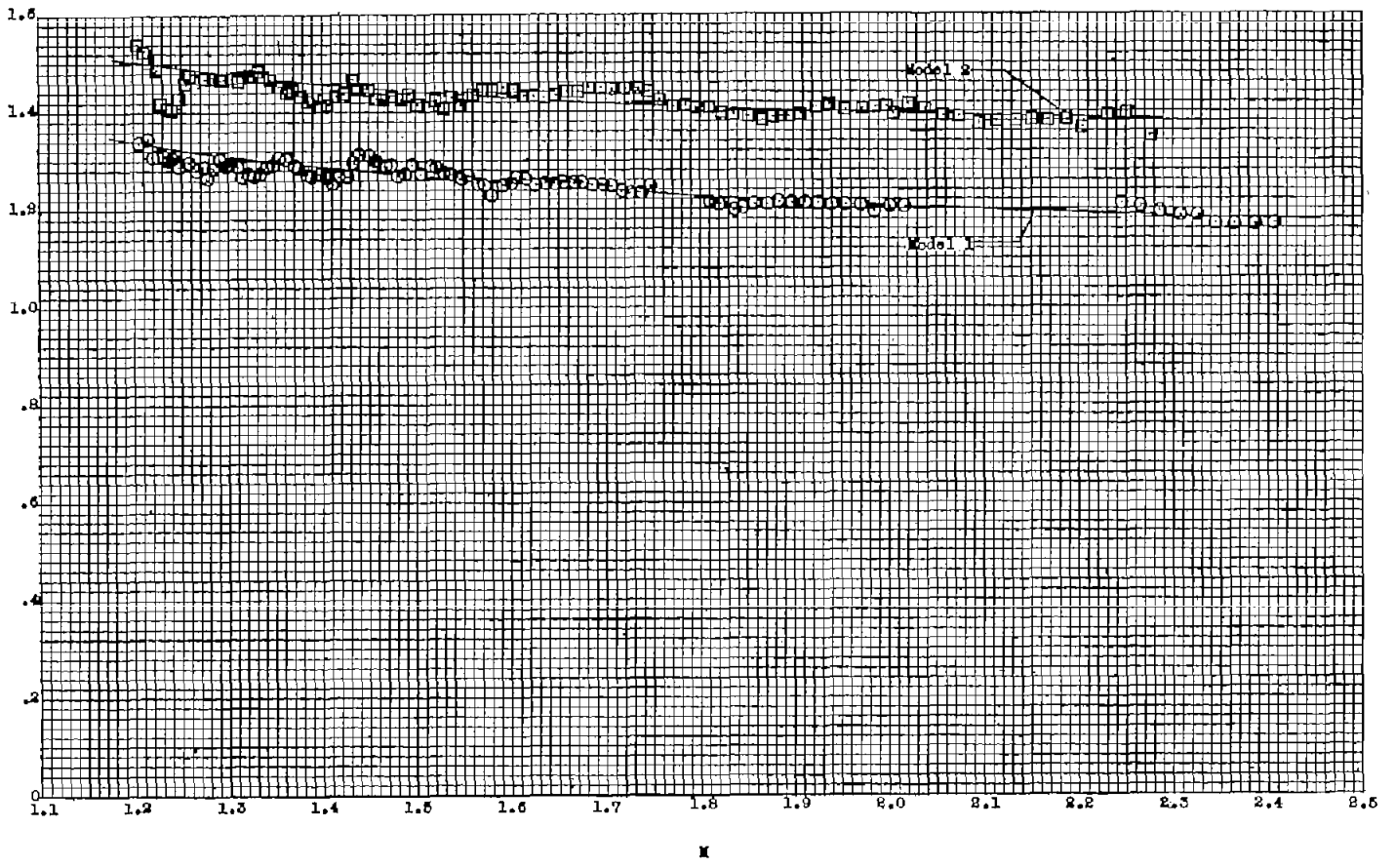

Figure 20.- Variation of drag coefficient with Mach number for models 1 and 2.